# Polyelectrolyte microcapsules for light triggered therapy and imaging

## Catarina Lourenço Costa

Thesis to obtain the Master of Science Degree in

## Biological Engineering

Supervisor: Doctor Suzana Maria de Andrade Sousa Paiva

Co-Supervisor: Doctor Vanda Isabel Roldão Vaz Serra

## Examination Committee

Chairperson: Prof. Maria Ângela Cabral Garcia Taipa Meneses de Oliveira

Supervisor: Doctor Suzana Maria de Andrade Sousa Paiva

Members of the Committee: Prof. Ana Rosa Galego Garcia

## September of 2020

## DECLARATION

I declare that this document is an original work of my own authorship and that it fulfils all the requirements of the Code of Conduct and Good Practices of the Universidade de Lisboa.

## PREFACE

The present work in this Thesis was performed at the Centro de Química Estrutural of Instituto Superior Técnico (Lisbon, Portugal), during the period September 2019 to June 2020, under the supervision of Dr. Suzana Maria de Andrade Sousa Paiva.

# AKNOWLEDGEMENTS

## RESUMO

Tendo em vista o desenvolvimento de um mecanismo de transporte adequado de porfirinas e aumento da eficiência da terapia fotodinâmica e a sua potencial aplicação em bioimagem, foram desenvolvidas microcápsulas com revestimento específico. Diferentes sistemas duplamente funcionalizados com um fotossensibilizador porfirínico, *meso*-tetrakis(*p*-sulfonatophenyl)porphyrin (TSPP), e rodamina 6G foram construídos – sistemas híbridos. A incorporação de rodamina tem o objetivo de promover o aumento de fluorescência do fotossensibilizador, por si só um fraco emissor, por transferência não radioativa de energia (processo conhecido por FRET,  Resonance Energy Transfer). O efeito da posição relativa porfirina/R6G na estabilidade dos sistemas gerados layer-by-layer foi estudada, e por FLIM verificou-se transferência de energia entre as duas espécies integradas na matriz de polieletrólitos adsorvida nas microcápsulas. A adsorção de polieletrólitos contrariamente carregados foi seguida por medição do potencial zeta. A funcionalização e caracterização das propriedades óticas e eletrónicas do sistema híbrido foi seguida por fluorescência de estado estacionário e resolvida no tempo e comparada com os sistemas contendo apenas porfirina ou rodamina, e com as mesmas espécies em solução. A aquisição de imagens por microscopia confocal de tempos de vida de fluorescência (FLIM) permitiu observar transferência de energia, responsável por excitar a porfirina que por sua vez, em ambientes oxigenados pode prosseguir por uma via fotoquímica que envolva transferência de energia entre o estado excitado tripleto do fotossensibilizador e oxigénio tripleto, produzindo uma espécie muito reativa com ação citotóxica eficiente, o oxigénio singleto.

Palavras-Chave: Microcápsulas, Polieletrólitos, Porfirina, Rodamina, Terapia Fotodinâmica, Bioimagem.

ABSTRACT

Aiming the development of an adequate mechanism for the transport of porphyrins, increasing the efficiency of photodynamic therapy and its potential application in bioimaging, microcapsules were developed with specific coating. Different double functionalized systems with a porphyrinic photosensitizer, *meso*-tetrakis (*p*-sulfonatophenyl) porphyrin (TSPP), and rhodamine 6G were built - hybrid systems. The incorporation of rhodamine has the objective of promoting the increase in fluorescence of the photosensitizer, itself a weak emitter, by non-radioactive energy transfer (a process known as FRET, Förster Resonance Energy Transfer). The effect of the porphyrin / R6G relative position on the stability of the layer-by-layer generated systems was studied, and by FLIM, energy transfer was verified between the two species integrated in the polyelectrolyte matrix adsorbed in the microcapsules. The adsorption of oppositely charged polyelectrolytes was followed by measurement of the zeta potential. The functionalization and characterization of the optical and electronic properties of the hybrid system was followed by steady-state fluorescence and resolved over time and compared with systems containing only porphyrin or rhodamine, and with the same species in solution. The acquisition of images by fluorescence confocal life time microscopy (FLIM) allowed to observe energy transfer, responsible for exciting porphyrin, which in turn, in oxygenated environments can proceed by a photochemical pathway involving energy transfer between the excited state photosensitizer triplet and triplet oxygen, producing a very reactive specie with efficient cytotoxic action, singlet oxygen.

Keywords: Microcapsules, Polyelectrolytes, Porphyrin, Rhodamine, Photodynamic Therapy, Bioimaging

TABLE OF CONTENTS

Table of Tables

Table of Figures

## LIST OF ABBREVIATIONS

| | |
|---|---|
| a.u. | Arbitrary units |
| $CaCO_3$ | Calcium carbonate |
| EDTA | Ethylenediaminetetraacetic acid |
| FLIM | Fluorescence lifetime imaging microscopy |
| FRET | Förster resonance energy transfer |
| $H_2O_2$ | Hydrogen peroxide |
| H-bonding | Hydrogen bonding |
| HCl | Hydrochloric acid |
| HOMO | Highest occupied molecular orbital |
| IC | Internal convertion |
| ISC | Intersystem crossing |
| LbL | Layer-by-layer |
| LUMO | Lowest unoccupied molecular orbital |
| MC | Microcapsule |
| $Na_2CO_3$ | Sodium carbonate |
| NaCl | Sodium chloride |
| NaOH | Sodium hydroxide |

| | |
|---|---|
| OD | Optical density |
| PAH | Poly(allylamine hydrochloride) |
| PDT | Photodynamic therapy |
| PE | Polyelectrolyte |
| PSS | Polystyrene sulfonate |
| TCSPC | Time-correlated single photon counting |
| TEM | Transmission electron microscopy |
| TSPP | Meso-tetra(4-sulfonatophenyl)porphyrin |
| Uv/vis | Ultraviolet/visible light |
| ROS | Reactive oxygen species |
| WHO | World Health Organization |
| %v/v | Volume fraction |

1.  INTRODUCTION

In 2018, Portuguese population registered around 58 199 cancer cases, from which 28 960 resulted in human loss, the highest mortality cancers are colorectum (14.7%) and lung cancer (16.1%). Globally, according to World Health Organization (WHO), cancer represents the second leading cause of death, accounting for an estimated 9.6 million deaths, or one in six deaths, in 2018. [1] Cancer patients globally do not have equal access to timely quality diagnosis which plays a vital role in their successful treatment and recovery. Currently available detection methods such as biopsy procedures, blood tests, and diagnostic tests, namely Computed Tomography (CT) and Magnetic Resonance Imaging (MRI) scans, are highly costly, time-consuming, with complex operations that require skilled personnel to operate. [2]

Depending on the type and stage of cancer, the selection of appropriate treatment often requires the use of multi-treatment modalities, like surgery and chemotherapy. Surgery can imply infections damaging the nearby tissues and is not effective for metastasis. Chemotherapy is a standard cancer therapy, however, due to poor targeting and lack of selectivity of this treatment, it damages healthy cells, the patients develop resistance to chemical agents, and have considerable toxic and severe side effects. Thus, it has become an urgent need to develop new economically viable cancer therapies and detection methods, to be applied with spatial-, temporal- and dosage-controlled ways on the early stages of this disease. [2]

Photodynamic Therapy (PDT) addresses some drawbacks of the nowadays available treatments, with lack of long-term toxic effects, and minimal invasiveness, this therapy has given a positive glance towards the research activity in the field, aiming its improvement. Porphyrins are a unique and diverse class of compounds widely available in nature, offering a variety of opportunities spanning various diagnostic and therapeutic modalities, applied in PDT as photosensitizers. By taking advantage of their known tuneable specific composition and reproducible synthesis, photophysical properties, biocompatibility, and biodegradation, with shown preferential retention on tumour tissues they provide functionalities as cargo tracking and activatable phototoxicity.[3] Upon sufficient accumulation of a porphyrin agent in the area of interest, followed by irradiation, there's a localized generation of reactive oxygen species (ROS) that evoke a cytotoxic effect of the target tumor tissue.[4]

Poor solubility in aqueous solutions at physiological pH, and the self-aggregation phenomena prevents intravenous delivery of porphyrins directly into the bloodstream, to address this challenge, microcapsules delivery vehicles systems arise. Colloidal carriers for porphyrins like polyelectrolyte multilayer microparticles, offer benefits of hydrophilicity, and appropriate size for enhanced permeability and retention on tumoral tissues.[4] The possibility of active targeting by using surface modification is also an attractive trait of these carriers, since they may be engineered with a light sensitive dye, like rhodamine, to enhance fluorescence for imaging and regulate the process of diffusion. Relatively to the porphyrin, this molecule has a small size and a high diffusion coefficient. [5][6] After being excited the rhodamine might promote the increase of the porphyrin's fluorescence, by transfer of excitation energy through a mechanism known as Förster Ressonance Energy Transfer. The excitation energy acceptor molecules of porphyrin are involved in the generation of ROS, like singlet oxygen, aiming the tumor cell death.

## 1.1. Polyelectrolyte Multilayer Microcapsules

Polyelectrolyte (PE) multilayer capsules engineered with active elements for targeting, labelling, sensing, and delivery represent a great promise for controlled delivery of drugs and the development of new sensing platforms. These biodevices should be biocompatible materials, like CaCO3 colloid templates, coated with specific functionalization, like porphyrin and rhodamine, that once exposed to a specific stimulus (e.g., pH variation, or light irradiation), undergo a gradual degradation of the shell components, leading to the release of the encapsulated cargo (e.g., enzymes, DNA and drugs). The integration of imaging agents, like the dye rhodamine 6G, for real-time tracking of a carrier's distribution, drug concentration, or release kinetics, gives this system a monitoring ability.[4][6]

PE hollow capsules (figure 1) are produced by Layer-by-Layer (LbL) assembly of oppositely charged polyelectrolytes onto colloidal particles, followed by the removal of the template core. It is generally accepted that the electrostatic interaction occurring between oppositely charged polyelectrolytes is the principal driving force for multilayer assembly, as well as the principal factor behind their stability. PE capsules properties, including size, shape, and the surface layers can be modified to alter the functionality of the capsule, or to improve colloidal stability.[7]
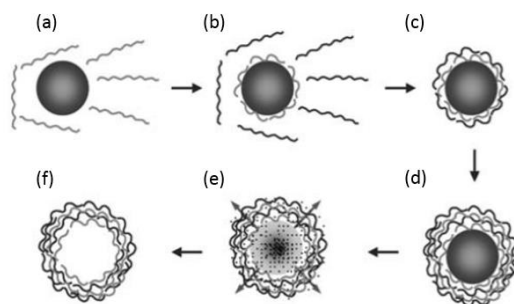


Figure 1. Scheme of polyelectrolyte hollow capsule preparation. The PE shell deposition of oppositely charged polyelectrolytes (negative- grey, and positive-black), in a spherical particle template (a-e). Hollow microcapsule preparation, after template destruction (f).(adapted)[7]

Generally, PE shells evidence selective permeability, high molecular weight compounds are hindered by the polyelectrolyte shell, whereas small molecules, as dyes, can penetrate the microcapsule shell.

### 1.1.1. Template cores

Different colloidal templates have been introduced for the fabrication of such microcapsules, including melamine formaldehyde, polystyrene latex, biological cells, poly-lactic/glycolic acid (PLA, PLGA) particles, inorganic substrates (such as $MnCO_3$, $CaCO_3$, $CdCO_3$) particles, and silicon dioxide ($SiO_2$) and gold particles.

Calcium carbonate ($CaCO_3$) particles constitute biocompatible and biodegradable templates, their synthesis is cost-effective, and do not require the use of any organic solvents. Towards removal of the core template, creating the hollow capsule, this inorganic substrate has the advantage that upon dissolution with an ethylenediamine tetraacetic acid (EDTA) solution, the metal ions are

complexed and can pass through the membrane of the polyelectrolyte shell. These capsules are known for their permeability to molecules with a molecular weight below 5 kDa and should, therefore, have no osmotic stress, preventing the destruction of the polymeric shell. Nonetheless, upon addition of $CO_2$ is formed causing an increase of the osmotic pressure, which perturbs the PE shell.[8][9]

### 1.1.2. Coating

For the shell-forming polyelectrolytes, the driving force for multilayer formation is the electrostatic attraction between the oppositely charged polyelectrolytes. Most studies have been performed with alternating poly(sodium 4-styrenesulfonate) (PSS) and poly(allylamine hydrochloride) (PAH), figure 2 (a) and (b), respectively. Factors such as pH and ionic strength, can largely tune the electrostatic interaction, and thus can be utilized to modulate the permeability and thickness. Besides the normal polyelectrolytes, various substances like optical brightening agents can also be incorporated into the system either on the capsule shells or within the capsules. [10]
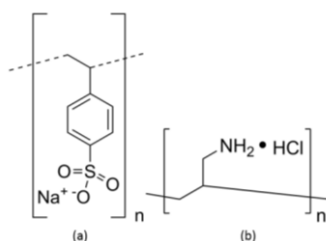


Figure.2. Chemical structures of (a) PSS and (b) PAH polyelectrolytes.

### 1.2. Photodynamic Therapy and Imaging

Photodynamic therapy (PDT) is a therapy approach for the followed destruction of a given biological target (e.g., cells or tissue) through the action of two per se harmless components, a photosensitizer (PS) and visible light. After tumoral loci PS accumulation, followed by irradiation, there is a localized generation of reactive oxygen species (ROS) that evoke cytotoxicity leading to cell death, or destruction of the target tissue. [11][12]

PDT is selective, since the generation of ROS only occurs upon irradiation of the sensitizer, hence the damage can be restricted to the irradiated area. Selectivity derives both from PS affinity to tumoral tissue and the precise delivery of light to tumoral tissue. Paradoxically, the highly localized nature of PDT is one of its current limitations, because the treatment is ineffective against metastatic lesions. PDT can also be used in combination with other therapies as chemotherapy, radiotherapy, or surgery without compromising these therapeutic modalities. None of the clinically approved PSs accumulate in cell nuclei, limiting DNA damage that could be carcinogenic or lead to the development of resistant clones. The only adverse effects of PDT relate to pain during some treatment protocols and a persistent skin photosensitization that has been circumvented by

the newer agents. The choice of optimal combinations of PSs, light sources, and treatment parameters are crucial for following a successful PDT. [13]

### 1.2.1. Photophysics and Photochemistry

Absorption of light leads to excitation of the PS molecule from its ground singlet state ($S_0$), to excited singlet state ($S_1$). The singlet state PS is very unstable and can undergo radiative (fluorescence), or nonradiative (internal conversion route) decay to come back to ground state. Alternatively, an excited PS may undergo an intersystem crossing, with spin inversion, achieving a triplet state ($T_1$). Triplet state relaxes back to ground state via phosphorescence pathway, or by internal conversion (radiationless transitions during collisions with other molecules). In oxygenated environments the PS can persue a Type II photochemical process which involves an energy transfer between excited triplet state of the PS and stable triplet oxygen ($^3O_2$), producing short lived and highly reactive singlet oxygen ($^1O_2$). Singlet oxygen is considered to be a proficient cytotoxic agent. Type I process requires electron or proton transfer, when the triplet state of PS interacts with biological substrates resulting in the formation of radicals and radical ions which on interaction with molecular oxygen gives rise to cytotoxic species like superoxide anion ($O_2^{\cdot-}$). Dismutation or one-electron reduction of superoxide anion results in hydrogen peroxide ($H_2O_2$), which in turn can undergo one-electron reduction to a powerful and virtually indiscriminate oxidant hydroxyl radical ($^\cdot OH$). It is generally accepted that Type II mechanism predominates during PDT but it was found that at low oxygen concentrations and in more polar environments Type I mechanism plays an important role, figure 3.[14]
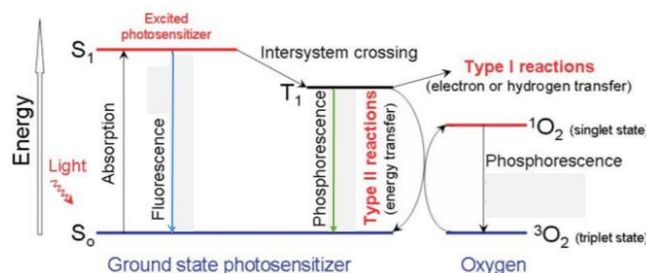


Figure 3. Modified Jablonski Diagram illustrating photosensitization processes. Light exposure takes the PS molecule from ground singlet state ($S_0$) to an excited singlet state ($S_1$), from which may undergo intersystem crossing to an excited triplet state ($T_1$) and then either form radicals via Type I reaction or transfer its energy to molecular oxygen ($^3O_2$) and form singlet oxygen ($^1O_2$), the major cytotoxic agent involved in PDT.

PDT can evoke some cell death pathways: apoptotic, necrotic, and autophagy-associated cell death. Apoptosis is a generally major cell death modality in cells responding to PDT. Although there is no specific cellular enzyme that can directly detoxify $^1O_2$, enzymes involved in other ROS metabolism may decrease the cytotoxic effect of PDT. Superoxide dismutase (SOD) increased activity has also been observed in various cancer cell types after PDT, comprising one of the protective mechanisms for cancer cells to avoid the cytotoxic effect.[15]

### 1.2.2. Light Source

When it comes to the light source, blue light penetrates least efficiently through tissue, whereas red and infrared radiations penetrate more deeply. The region between 600 and 1200 nm is often called the optical window of tissue. Nevertheless, only wavelengths up to 800 nm can generate reactive singlet oxygen ($^1O_2$). The choice of the light source, exposure time, and delivery mode should, therefore, be based on PS absorption (fluorescence excitation and action spectra), disease (location, size of the lesion, accessibility, and tissue characteristics), cost, and size. Diode lasers are being specifically designed for PDT since they are cost-effective, simple to install, have automated dosimetry and calibration features, and longer operational life.[16]

### 1.2.3. Porphyrins as photosensitizers

An ideal PS is required to be chemically pure with known specific composition and reproducible synthesis, to allow quality control analysis with low manufacturing costs and good stability in storage. Its quantum yield for singlet oxygen production should be high and it should have a strong absorption peak preferably between 600-800 nm, where scattering of light is minimum and tissue penetration is maximum . (3 to 8 nm depth penetration can be achieved for light in the 630 - 800 nm range), and photons provide enough energy to produce singlet state oxygen. The PS should be easy to dissolve in the body's tissues, capable of formulation (dissolution in injectable solvents), have no dark toxicity, and rapid clearance from healthy tissues minimizing phototoxic effects. [16][17].

Porphyrins, aromatic, organic, light-absorbing molecules that occur abundantly in nature, especially in the form of molecular self-assemblies, are among the most successful PDT agents. Their preferential accumulation mechanisms in tumor cells are explained based on low-density lipoprotein receptors theory and pH difference. Lipophilic porphyrins bind to the centre of low-density lipoprotein receptor, entering tumour cells through a specific membrane receptor, apolipoprotein B. Additionally, it was pointed out that tumour tissues have lower pH (5.85-7.68) values than healthy tissues (7.0-8.0) because of their faster metabolism. Porphyrins enter cells by passive diffusion, this diffusion would efficiently increase with the decrease of pH values. The larger the tumor tissue, the lower the pH values, which facilitates preferential aggregation of porphyrins in tumor tissues.[18] [19]

Hematoporphyrin derivatives (HPDs) were the first photosensitizers being studied, Photofrin® derived from HPDs and was the first PS approved by Food and Drug Administration (FDA). It is the most frequently used PS for the treatment of oesophageal cancer, bladder cancer and gastric cancer. Although being approved, the so-called first-generation PS had some unfavourable characteristics: : it was isolated as a mixture of different chemical species (mixture of oligomers formed by ether and ester linkages of up to eight porphyrin units), it had limited tissue penetration (only to superficial lesions) its poor absorption at 630 nm, and caused long lasting photosensitivity of the skin.

To solve some of these problems, research came up with a second-generation PSs, figure 4: porphyrin and porphyrin analogue photosensitizers such as Hemoporfin® (porphyrin), Foscan®, Visudyne® (chlorin), Tookad® (bacteriochlorin) and Photocyanine® (phthalocyanine).[20][21]
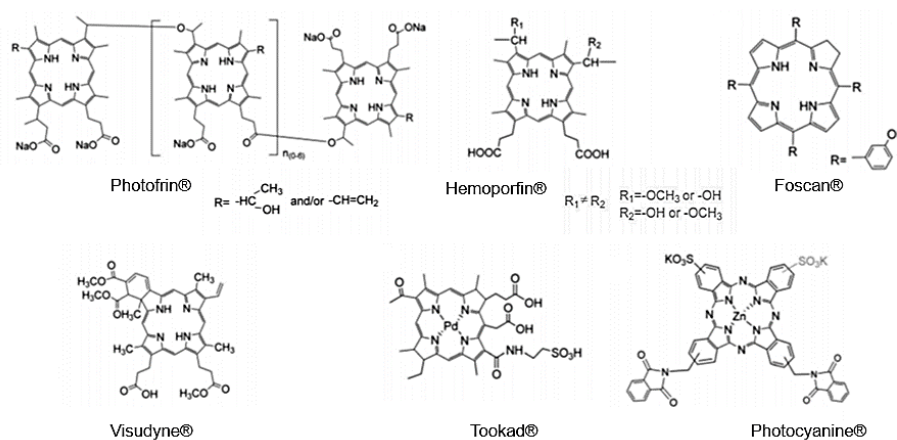


Figure 4. Structural formula of second-generation porphyrinic photosensitizers commonly used clinically.

Whilst being clinically used for certain indications, the second-generation PSs pose some drawbacks. On the one hand, Hemoporfin® has limited ability to treat deep biological tissues and Foscan® forms aggregates after injection causing severe inflammations due to poor solubility, on the other hand Visudyne® is considered safe to treat vertebral metastases, both from a pharmacological and neurological perspective. Tookad® and Photocyanine®, are amphiphilic photosensitizers, both considered safe, effective, and quality controllable (table 1). The first one is activated at longer wavelengths, treating deep tumoral tissues, and has a good elimination rate after treatment. Compared with the first-generation porphyrin PSs, the second-generation PSs presents higher absorption in the near-infrared spectral region, better ROS production efficiency, faster accumulation within the tumoral tissues, easier elimination from healthy tissue, and lower skin photosensitivity. [22]

Table 1. Porphyrinic compounds as photosensitizers in clinical trials. Photofrin® is a first-generation PS, the other PSs mentioned belong to the second-generation.

| Macrocycle compound platform | Photosensitizer | Trade name | Excitation wavelength | Manufacturer | Potential indications |
|---|---|---|---|---|---|
| Porphyrin | Hematoporphyrin derivatives | Photofrin® | 630 nm | Axcan Pharma, Canada | Esophageal cancer, bladder cancer, gastric cancer, bronchial cancer |
| | Hematoporphyrin derivatives | Hemoporfin® | 630 nm | Fudan Zj, China | Port wine stains, early gastric cancer and rectal cancer |
| Chlorin | Temoporfin | Foscan® | 652 nm | Biolitec, Germany | Prostate cancer, head and neck cancer, pancreatic cancer |
| | Verteporfin | Visudyne® | 690 nm | Novartis, Switzerland | Age related macular degeneration, vertebral metastases |
| Bacteriochlorin | Padeliporfin | Tookad® | 763 nm | Steba Biotech, UK | Prostate cancer |
| Phthalocyanine | Suftalanzinc | Photocyanine® | 676 nm | Longhua Pharm, China | Gastrointestinal cancer, colon cancer, esophageal and nasopharyngeal cancer solid tumors |

1.2.3.1. Porphyrin structure and properties

Porphyrins represent a class of macrocycles comprised of four pyrrole units interconnected at their α-carbon atoms, conjugated through methine bridges (=CH-). When a metal ion (such as iron, magnesium, zinc, or cobalt) is attached at their centre, the compound is said to be a metalloporphin. When two hydrogen atoms are attached, the compound is termed as a free base porphin. The periphery of these structures contains hydrogen atoms that can readily be displaced by one or more molecular groups, thus forming the general class of porphyrins. Porphine, does not occur in nature and is used for theoretical interest, it's the most fundamental cyclic tetrapyrrole, with no peripheral chains, considered the starting material of various porphyrin derivatives. Porphyrins can be functionalized at the meso and β positions, figure 5.
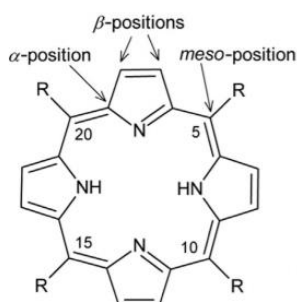


Figure 5. Chemical structure of porphyrin nuclei.

Porphyrins are 2D aromatic systems, and it is assumed that 18 of their 22-π electrons are delocalized, obeying to the Huckel rule (4n+2). The simplest interpretation of porphyrin electronic absorption spectra is given by Martin Gouterman in 1959, with the "four-orbital" model. [23]

According to this model, the absorption bands in porphyrin systems arise from π-π* (π, occupied and π*, unoccupied) transitions between two HOMO (Highest Occupied Molecular Orbitals) and two LUMO (Lowest Occupied Molecular Orbitals) orbitals, figure 6.
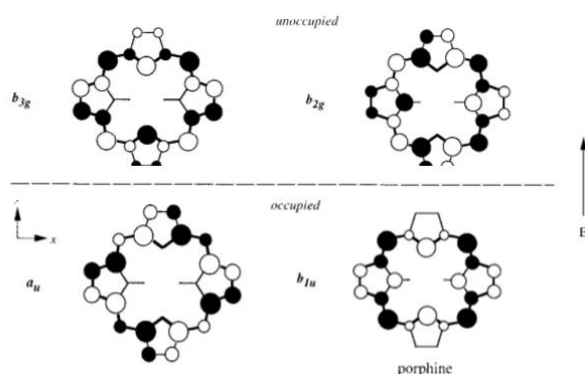


Figure 6. HOMO (au), next HOMO (b1u), LUMO (b2g) and next LUMO (b3g) orbitals of free base porphyrin.

Considering HOMO ($a_u$), next HOMO ($b_{1u}$), LUMO ($b_{2g}$), and next LUMO ($b_{3g}$); ($a_u$, $b_{2g}$) and ($b_{1u}$, $b_{3g}$) are called a conjugated pair of orbitals. Due to their pairing property the energy of the configuration obtained by exciting an electron from the orbital $a_u$ to the orbital $b_{3g}$ is equal to that obtained by excitation from $b_{1u}$ to $b_{2g}$. The linear combinations of the two degenerate

configurations generate the minus (-) and plus (+) states. The "minus state" is a covalent state whereas the plus state is an ionic state that happens when both transitions occur between a conjugated pair of orbitals and they mix with same sign. The HOMO→LUMO ($a_u$→$b_{2g}$) excitation gives rise to the lowest $2^1B_{2u}{}^+$ state with ionic nature. The two single excitations of $a_u$->$b_{3g}$ and $b_{1u}$→$b_{2g}$ result in a pair of covalent $2^1B_{3u}{}^-$ and ionic $1^1B_{3u}{}^+$ states. The electric dipole transition moment vectors for the one-electron $a_u$→$b_{3g}$ and $b_{1u}$→$b_{2g}$ transitions are similar in magnitude and parallel in their orientation. For $a_u$→$b_{2g}$ transitions, the dipole transition moment vector is antiparallel to that for $b_{1u}$→$b_{3g}$. Thus, the transition to $2^1B_{3u}{}^-$ is parity forbidden, whereas transitions to $2^1B_{2u}{}^+$ and $1^1B_{3u}{}^+$ are dipole-allowed. The ground state of free base porphyrin is $^1A_{1g}$.

Four excited electronic configurations can be built: $(a_u)^2(b_{1u})^1(b_{2g})^1(b_{3g})^0$; $(a_u)^2(b_{1u})^1(b_{2g})^0(b_{3g})^1$; $(a_u)^1(b_{1u})^2(b_{2g})^1(b_{3g})^0$ and $(a_u)^1(b_{1u})^2(b_{2g})^0(b_{3g})^1$. Leading to four excited electronic states: to four $1^1B_{3u}$, $1^1B_{2u}$, $2^1B_{3u}$, $2^1B_{2u}$, figure 7.
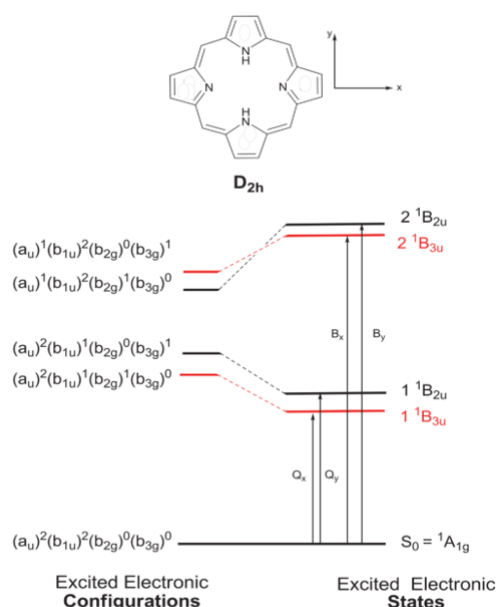


Figure 7. Molecular orbital diagram and molecular states for free base porphyrins D2h. Each electronic transition originates spectral bands, B band (very intense) arises from the linear combination of two transitions with reinforcing transition dipoles; Q bands result from transition dipoles nearly cancel each other out.

The Q and B bands arise from a linear combination of these one-electron transitions. For the lower Q-band, the transition dipoles nearly cancel giving rise to the relatively weak absorption in the visible region. For the higher energy B-band, the transition dipoles reinforce, resulting in the very intense absorption in the UV region.

The weakness of the Q-band is due to the alternance symmetry. The transitions which give rise to the lower component of the Q-band ($1^1B_{3u}$) are $a_u$→$b_{3g}$ and $b_{1u}$→$b_{2g}$ and they mix with a different sign. These transition dipole moment vectors are almost the same in magnitude and parallel in their orientation, leading to the cancelation of their intensities. A similar cancelation also occurs in the upper component ($2^1B_{2u}$) which has the main transitions of $a_u$→$b_{2g}$ and $b_{1u}$→$b_{3g}$. As

a result of the alternance symmetry, the transitions are parity forbidden, resulting on the weakness of the Q-band in a free base porphyrin. Chemical modifications such as external substituents, changes in conjugation pathway, and change in central substituent can increase the intensity of the Q-band.

The third valence excited state is the $2^1B_{3u}$ state. The state can be described by the single transitions of $a_u \rightarrow b_{3g}$ and its conjugate. In this case two transitions mix with the same sign. The $a_u \rightarrow b_{3g}$ and $b_{1u} \rightarrow b_{2g}$ transition dipoles are reinforced, resulting in the strong optically allowed absorption in the near UV region. Theory predicted the fourth valence excited state to be the $2^1B_{2u}$, this state is described by a linear combination of singly excited configurations of $b_{1u} \rightarrow b_{3g}$ and $a_u \rightarrow b_{2g}$. In contrast to the $1^1B_{2u}$ state, the mixing coefficients are minus. The addition of the dipole moments occurs in this state and the oscillator strength is again very intense. The B -bands or Soret bands of free base porphyrins consist of two separate transitions from the ground state to the $2^1B_{3u}$ and $2^1B_{2u}$ states. Both states are ionic and the transitions are optically strongly allowed.

Upon complexation with a metal ion, the number of Q bands decreases due to the molecular symmetry shifts from rectangular $D_{2h}$ to square $D_{4h}$ in going from free base porphyrin to metalloporphyrins. The $b_{2g}$ and $b_{3g}$ orbitals in the $D_{4h}$ metalloporphyrins are enforced to be degenerate ($e_g$ orbitals degenerate into $e_{gx}$ and $e_{gy}$), figure 8. [25][26]
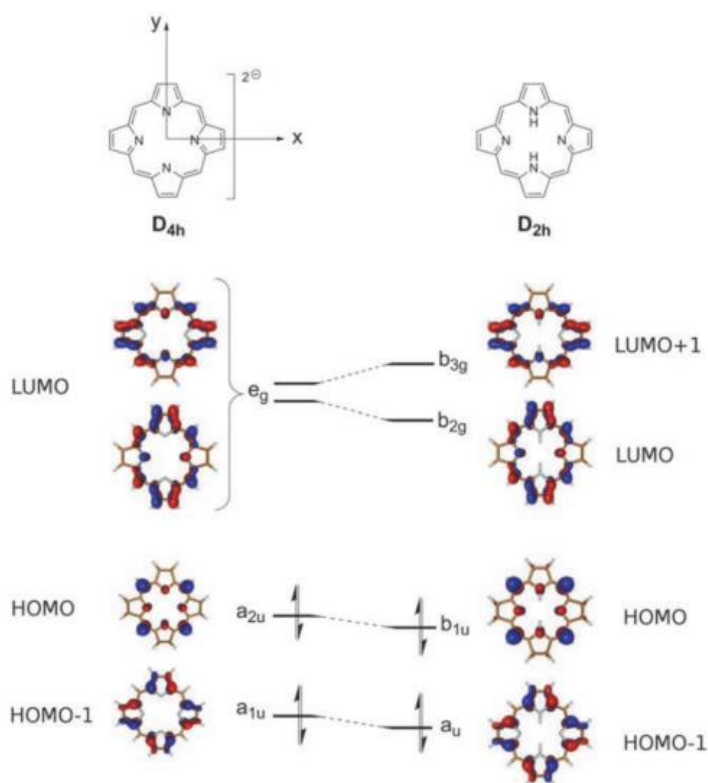


Figure 8. Four orbitals of the Gouterman model of $H_2P$ (in $D_{2h}$ symmetry) deduced from the molecular orbitals of $P^{2-}$ (in $D_{4h}$ symmetry).

The Soret or B band, is displayed at about 400 nm, Q bands, are displayed in the range between 500-750 nm (the $Q_{IV} \rightarrow Q_I$ bands), figure 9.
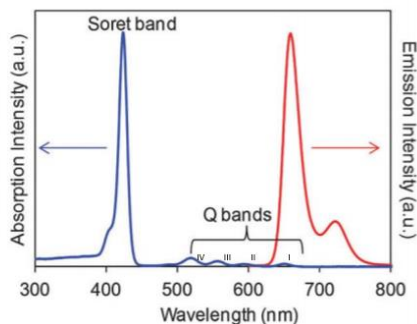


Figure 9. UV-Vis absorption spectra (blue), and emission spectra (red) of a free base porphyrin.

The fluorescence emission spectra of porphyrins is easily detected by excitation at the Soret's wavelength (~400nm), comprised by two bands ~650 nm and ~720 nm in the red region.

The aggregation of porphyrins in aqueous solution is dependent on physical-chemical characteristics, such as ionic strength, pH and solvent composition. These self-assembly processes are natural and might be driven by several types of non-covalent interactions, namely π-π stacking, electrostatic interactions, hydrogen bonding and van der Waals interactions, facilitating long-range association in which the mixing of electronic excited states generates new optical properties. J-aggregates, result from side-to-side coupling of transition dipoles, leading to a red shift of the Soret and Q absorption bands. In turn, H-aggregates, which result from porphyrin face-to-face coupling (π-π stacking), cause a blue shift of the Soret band.

### 1.2.3.2. *Meso*-(tetrakis)-(*p*-sufonatophenyl)porphyrin

*Meso*-(tetrakis)-(*p*-sufonatophenyl)porphyrin (TSPP) is an amphiphilic synthetic porphyrin and exists as a monomer in aqueous solution below 30 µM, with zwitterionic character over a wide pH range. Above pH 4.8, TSPP is a tetraanionic porphyrin with four sulfonatophenyl groups in the *meso* positions and a global net charge of -4. At lower pH values the protonation of the inner nitrogen occur, giving the inner core a global net charge of +2, and a global net charge of -2 ($H_4TPPS^{-2}$), figure 10. This porphyrin aggregation is specially triggered by acidic environments: the combination of H-bonding, intermolecular ionic interactions between anionic sulfonate groups and the positively charged nature of the macrocycle core of the neighbouring molecules are considered the driving forces for its self-assembly phenomena.
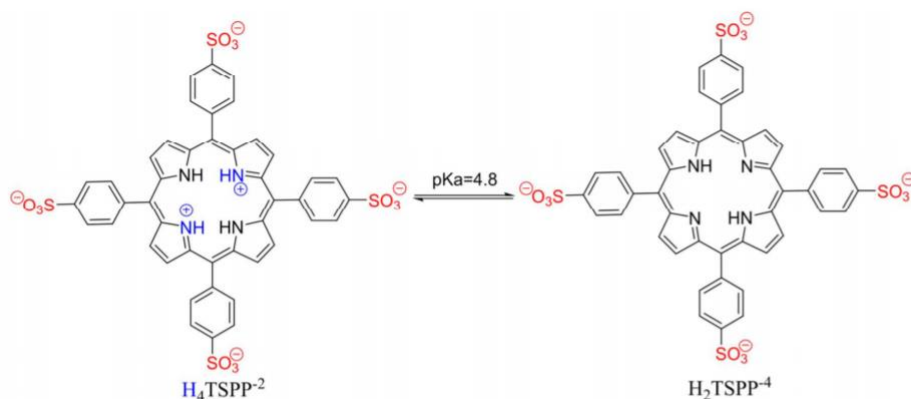
Figure 10. Acid-base equilibrium of TPPS in aqueous solutions.

By lowering the pH there's a symmetry change from $D_{2h}$ to $D_{4h}$ (due to NH protonation) and a red shift in the typical Soret band from 413 nm to 434 nm occurs, simultaneously with the non-splitting of the Q bands (from four to two). In these conditions there might be the emergence of a sharp red-shift peak at ~490 nm and a broad band at ~708 nm. These two bands are assigned to be monomers' coupling towards a J-aggregate arrangement. A broad band near 400 nm is a fingerprint of H- aggregation.

Porphyrins have been used to infer about highly efficient electron and energy transfer processes in biological systems. The main issue about these molecules is the control of their molecular orientation and to overcome the lack of robustness due to weak intermolecular forces involved that prevent their easy incorporation into devices The molecular aggregates formed have different emission dynamics from the ones seen with isolated molecules, due to the formation of Frenkel excitons, which are delocalized because of intermolecular coupling between molecules and the sharing of excitation gives rise to aggregates with electronic and spectroscopic unique features. These aggregates have been interpreted within the framework of exciton theory, where the dye is treated as a dipole and a splitting of excited state in two levels takes place. H- and J- aggregates are associated with their cofacial structure causing a blue-shifted Soret absorption and edge-to-edge structure, causing red-shifted Soret absorption, respectively. The origin of these features is assigned to the emergence of an excitonic state through the electronic coupling of tightly packed porphyrin units. These aggregates are therefore classified according to its orientation of the induced transition dipole of the constituent monomers based on their signatures in the splitting position of the Soret (figure 11).[26][27][28]
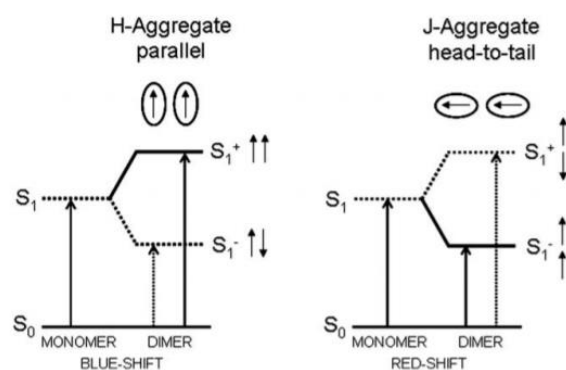
Figure 11. Exciton-coupling model to explain the spectral shifts relation with the orientation of the dyes' transition dipole moments.

### 1.2.4. Rhodamine

Fluorescent dyes applied in biological labelling offer many advantages, such as fast detection speed, good repetitiveness, low dosage, and non-radiation. Fluorescence microscopy is a simple non-destructive imaging and intracellular examination of biologically relevant processes technique, at high spatial and temporal resolutions. Assembling fluorescent dyes to PE capsules is a versatile way to create composition and geometry controllable platforms for drug-delivery. The dye molecules are entrapped between polyelectrolyte layers due mainly to electrostatic interactions. Such configuration allows for overcoming the high toxicity of dye molecules, such as rhodamine. The shell of each sensor capsules labelled by adding this sort of molecules enables real-time tracking of the drug-carrier to its target site and measurements of releasing of the interest analyte.

Rhodamines are xanthene derivate molecules and have excellent photophysical properties such as high molar absorptivity or molar extinction coefficient, high fluorescence quantum yield, high photostability and relatively long emission wavelength. Rhodamine 6G (R6G), figure 12, also known as Rhodamine 590, is a cationic dye widely used as a fluorescence tracer. At high concentration, the R6G molecules arrange themselves in so-called H-type and J-type dimers or larger aggregates, the first of which is energetically favoured. Summarily, the H-type dimer is a sandwich-like structure in which the 3-ring systems of two molecules are aligned in parallel, while assembling orthogonally to each other in the J-type conformation. The electronic absorption spectra of R6G aqueous solutions have the maximum absorption band around 526 nm due to R6G monomer, and a higher energy shoulder band at 495 nm due to the aggregates of R6G (the H dimer). These dimers are formed through van der Waals dye-dye interactions and rhodamine-water (counterions) interactions and their fluorescence emission band shows around 600nm, but at low dye concentration (below $10^{-5}$ M), most dye molecules are isolated from each other and fully solvated, hence the emission band appears around 560 nm.[29]
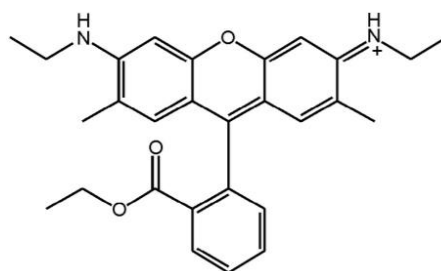
Figure 12. Chemical formulae of Rhodamine 6G, the counterion is Cl⁻.

## 1.3. Objectives

The aim of the present Thesis is to design a double functionalized polyelectrolyte, PSS and PAH, coated colloidal system with a porphyrinic photosensitizer, meso-tetrakis (p-sulfonatophenyl) porphyrin (TSPP), and rhodamine 6G .This microcapsules systems are expected to maintain the monomeric form of the photosensitizer (porphyrin), to prevent self-quenching, and further improve the selective aggregation of porphyrin in target sites to enhance the local anticancer effect. R6G expected role is to, upon excitation, transfer excitation energy by FRET to the acceptor molecules of TSPP. The success of this energy transference mechanism is related to the dipole orientation of both donor and acceptor molecules. Both polyelectrolytes, PSS and PAH might orientate the dipoles of the dyes' molecules in a favourable way, such that the FRET process is efficient.

## 2. EXPERIMENTAL

### 2.1. EXPERIMENTAL METHODS

#### 2.1.1. Light Absorption

Molecular electronic transitions are generally accompanied by simultaneous changes in vibrational and rotational states. Molecular internal energy, $E_{int}$, can be approximated as the sum of contributions from different energies, such as electronic, $E_{El}$, vibrational, $E_{Vib}$, and rotational, $E_{Rot}$, (1) and figure 13.

$$E_{int} = E_{El} + E_{Vib} + E_{Rot} \qquad (1)$$

The Born-Oppenheimer approximation is one of the basic concepts underlying the description of the quantum states of molecules. According to this approximation, since the mass of the electrons is much smaller than nuclear mass, electronic transitions are much faster than atomic motion.
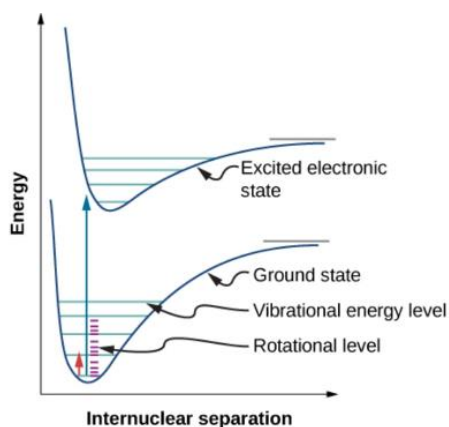


Figure 13. Three types of energy levels; electronic, vibrational, and rotational.

The Frank-Condon principle relates to the interaction between the electronic and vibrational motions and like the Born–Oppenheimer approximation follows from the fact that the nuclear masses are much larger than the electronic mass. This principle states that the electronic transitions, vertical transitions, are so rapid and their timescale is so fast when compared with the nuclear motion ($r$) that we may consider the nuclei to be fixed during the transition. The charge redistribution in a molecule that follows electronic transition causes changes in the vibrational state of the molecule. Simultaneous occurrence of electronic and vibrational transitions, called vibronic transitions, give rise to the vibrational structure of the electronic bands, figure 14. The quantum mechanical formulation of this principle is that the intensity of a vibronic transition is proportional to the square of the overlap integral between the vibrational wavefunctions of the two states that are involved in the transition ($\langle \Psi_v | \Psi_v^{ex} \rangle$-Frank Condon factor, this integral signifies the overlap of vibrational wave functions of the ground and excited electronic states). In figure, a case is illustrated in which maximum overlap occurs between the $v = 0$ and $v' = 2$ vibrational wave functions.[30]
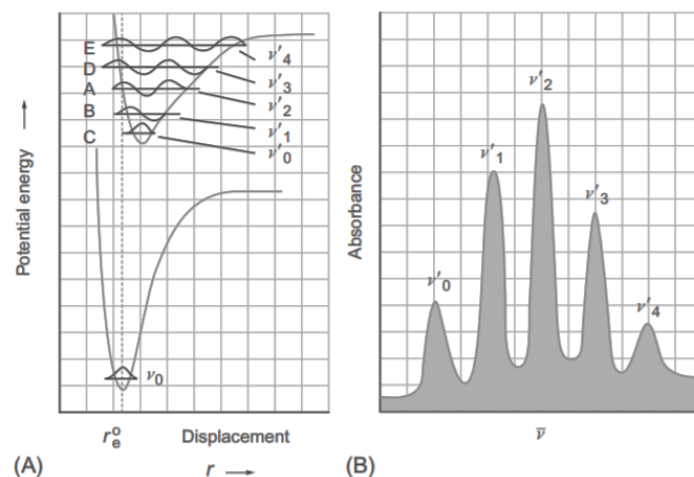
Figure 14. (A) Potential energy diagram for a diatomic molecule illustrating the Frank- Condon vertical transition (dashed line); illustration of maximal overlap between v= and v'=2 vibrational wave functions, level A, where the internuclear separations are nearly equal. (B) Excitations to the vibrational sublevels impose the shape of the electronic absorption band.

### 2.1.2. Fluorescence and competing Processes

Electronic transitions are vertical transitions that occur when there's the absorption of a photon by an atom or molecule, from its ground state energy level $S_0$, to a higher energy level, an excited state. The electronic states of most organic molecules can be divided into singlet states $S_n$, and triplet states, $T_n$, where all electrons in the molecule are spin paired or one set of electron spins is unpaired, respectively.

Jablonksi diagram, figure 15, is a powerful tool for visualising the possible electronic transitions, after molecular photoexcitation. Energy levels are shown by horizontal black lines, with increasing energy along the vertical axis of the diagram. Bold lines represent the lowest vibronic level of each electronic state, thinner lines are higher vibronic levels.

Upon absorption, the molecule is promoted from the lower vibrational energy of its ground state $S_{0, v=0}$ to a higher state, the singlet excited states ($S_1$, $S_2$, …). This is considered an instantaneous process ($10^{-15}$ s). The occupation of singlet states is controlled by the interaction of the electron involved in the transition with the electric field of the excitation light. The molecule will then eventually dissipate energy through two non-radiative ways: vibrational relaxation and internal conversion (IC). Vibrational relaxation, the transition to the lower vibrational level of the excited singlet $S_{1, v=0}$, ($10^{-12}$-$10^{-10}$s), occurs by losing energy to other molecules through collisions. The molecule might also undergo internal conversion (IC), transition to a lower singlet electronic state with the same spin multiplicity, $S_2$->$S_{1, v=n}$ ($10^{-11}$–$10^{-14}$ s).
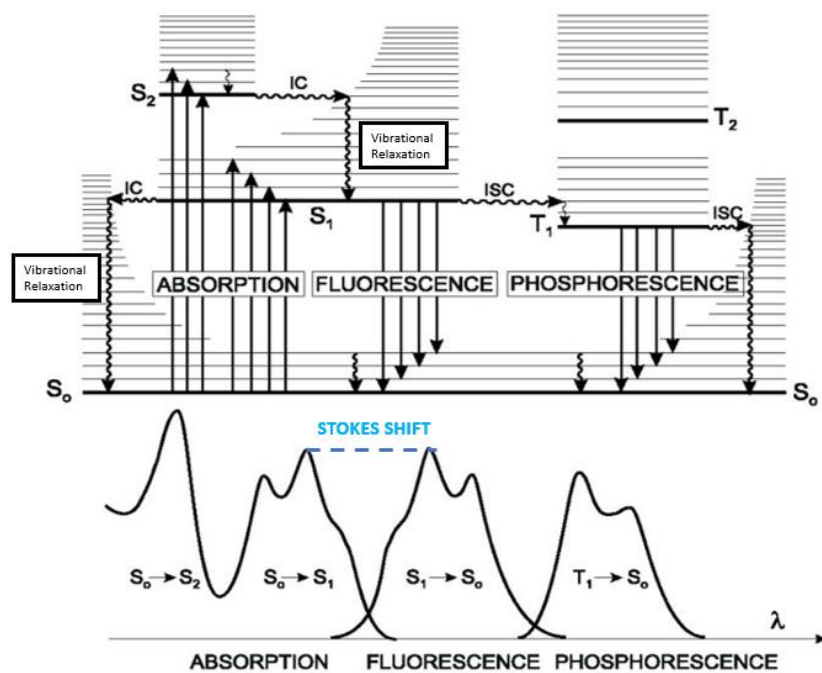
Figure 15. Perrin-Jablonski diagram. The molecular electronic states and photophysical processes are displayed. Vibrational energy levels are shown as thinner layers, radiationless transitions represented with curly arrows; vibrational relaxation, IC (internal conversion), ISC (intersystem crossing). Gap between absorption and emission is also shown, Stokes Shift.

The emission of photons might occur by spontaneous radiative transition known as fluorescence ($10^{-10}$-$10^{-7}$s). The non-radiative transition between two electronic states of different spin multiplicity ($10^{-11}$-$10^{-9}$s) is called intersystem crossing (ISC), and usually leaves the molecule in the first excited triplet state, T1. The $T_1 \rightarrow S_0$ transition is known as phosphorescence. Both ISC and phosphorescence, singlet-triplet and triplet-singlet transitions respectively, are forbidden. Although being less probable to occur, they are weakly allowed through spin-orbit coupling. In fact, because of this, phosphorescence occurs with a longer timescale than fluorescence ($10^{-6}$-1s).

Even though vertical excitations result in accommodation of the electron in upper electronic excited states, fluorescence occurs from the lowest lying electronically excited singlet state $S_{1, v=0}$ and phosphorescence from the lowest lying triplet state $T_{1, v=0}$ (Kasha's rule). The energy of the emission is typically lower than the absorption energy, since IC and vibrational relaxation phenomena dissipate the accumulated energy to the allowed singlet state for the fluorescence to occur. This difference between excitation and emission wavelengths is called Stokes shift. [31]

2.1.1.2. Fluorescence lifetimes and quantum yields

Quantum yield, $\phi_F$, is the number of emitted photons relatively to the number of absorbed photons. Molecules with the highest quantum yields (approximately $\phi_F = 1$), like rhodamines, display the brightest emission. Fluorescence lifetime, $\tau$, refers to the average time that a molecule

remains in the singlet excited state. As discussed above, the molecular excited state can decay through either radiative or non-radiative processes, characterized by decay rate constants $k_f$ and $k_{nr}$, respectively. $k_{nr}$ is given by the sum of the rate constants for IC from S1->S0 ($k_{IC}$), and for ISC ($k_{ISC}$). Thus, the quantum yield is calculated by the following expression:

$$\phi_F = \frac{k_f}{k_f+k_{nr}} \qquad (2)$$

Where, $k_{nr} = k_{IC} + k_{ISC}$ $\qquad$ (3)

The lifetime ($\tau$) is given by:

$$\tau = \frac{1}{k_r+k_{nr}} \qquad (4)$$

Conjugating both equations, is possible to obtain the relation between the quantum yield, $\phi_F$, and fluorescence lifetime $\tau$, as shown by the following equation:

$$\phi_F = k_r\,\tau \qquad (5)$$

The relative determination of Fluorescence Quantum Yield method relies on the comparison of integral emission spectra of a standard dye versus that of the sample being used, under identical conditions. The standard must have a known quantum yield and similar optical properties as the sample, and the use of the same cuvettes to minimize the effect of scattering losses at the interface. UV-vis emission spectra of sample and standard are obtained at a chosen wavelength, that acts as the excitation wavelength for emission spectra of both sample and standard. One should ensure maximum extinction values below 0.2. The quantum yield is calculated by:

$$\phi_x = \phi_{st} \frac{f_{st}}{f_x} \frac{F_x}{F_{st}} \frac{n_x^2}{n_{st}^2} \qquad (6)$$

Where underscripts st and x refer to the standard and the sample, respectively; $\phi$ is the quantum yield, $n$ identifies the refractive index of the solvent, $f$ is ibtained from the exctintion spectrum and represents the absorption factor, whereas $F$ is in units of photos and is the integral of the emission spectrum.

$$f = 1 - 10^{-A(\lambda exc)} \qquad (7)$$

$$F = \int_0^{\lambda_{em}} \frac{S1_c}{R1} d\lambda_{em} \qquad (8)$$

$A(\lambda_{exc})$ refers to the value of absorption at the chosen wavelength and $\frac{S1_c}{R1}$ the instrument wavelength dependence corrected emission spectrum.

### 2.1.3.  UV-Visible absorption spectroscopy

Lambert–Beer Law is a mathematical means of expressing how light, with wavelength λ is absorbed by matter. The absorbance or optical density, A (λ), is given by:

$$A(\lambda) = log\frac{I^0_\lambda}{I_t} = -\log T(\lambda) \qquad (9)$$

Where $T$ is the transmittance, given by

$$T(\lambda) = \frac{I_\lambda}{I^0_\lambda} \qquad (10)$$

Where $I^0_\lambda$ represents the photon incident intensity, and $I_\lambda$ the photon transmitted intensity.

Therefore, Beer-Lambert equation may also be written as

$$A(\lambda) = log\frac{I^0_\lambda}{I_t} = \varepsilon_\lambda\,l\,c \qquad (11)$$

From this, $\varepsilon_\lambda$ represents the molar extinction coefficient (or molar absorptivity) with units $M^{-1}cm^{-1}$, when the concentration, $c$, and the path length, $l$, are given in molarity, M, and cm, respectively.

Some deviations can arise from inhomogeneous samples, with dimerization or aggregation at higher concentrations, or changes in equilibrium. The most common consequence is that the measured absorbance does not increase linearly with increasing concentration or path length.

Considering the molecular scale, each molecule has an associated photon-capture area, called the molecular absorption cross-section $\sigma$, which is wavelength dependent. A thin layer of thickness $dl$ contains $dN$ molecules,

$$dN = N_a\,c\,S\,dl \qquad (12)$$

For the practical use of the Lambert-Beer Law the sample consists in a solution placed in a cuvette. Ideally, the absorbance is obtained exclusively due to the absorbing species being studied. We should note that $I_0$ is the intensity of the beam entering the solution, not the same as the incident beam, $I_i$, on the cuvette; moreover $I$ is the intensity of the beam leaving the solution different from the beam, $I_s$, leaving the cuvette, since there are some reflections and absorptions phenomena occurring (in a less extent) on the cuvette walls. It's considered that the solvent doesn't have any contribution to the measured absorbance, yet it may be partially responsible for a decrease in intensity because of scattering and possible absorption. The total absorbance of the sample and its cuvette walls is given by

$$A_s(\lambda) = log\frac{I_i}{I_s} \qquad (13)$$

Comparatively, the solvent cuvette absorbance is given by

$$A_R(\lambda) = log\frac{I_i}{I_R} \qquad (14)$$

The real absorbance is then calculated from the difference

$$A(\lambda) = A_R(\lambda) - A_R(\lambda) = log\frac{I_R}{I_S} \qquad (15)$$

Measurement of absorbance is usually performed in a parallel, double-beam method, figure 16, obtaining automatically the real absorbance value ($log \frac{I_R}{I_S}$). Firstly, the spectrophotometer records and stores a baseline, based on the solvent cuvette.[32][33]

$$A(\lambda) = log \frac{I_0}{I} = \varepsilon \ell c$$

$$A_S(\lambda) = log \frac{I_i}{I_S}$$

$$A(\lambda) = A_S - A_R = log \frac{I_R}{I_S}$$

$$A_R(\lambda) = log \frac{I_i}{I_R}$$
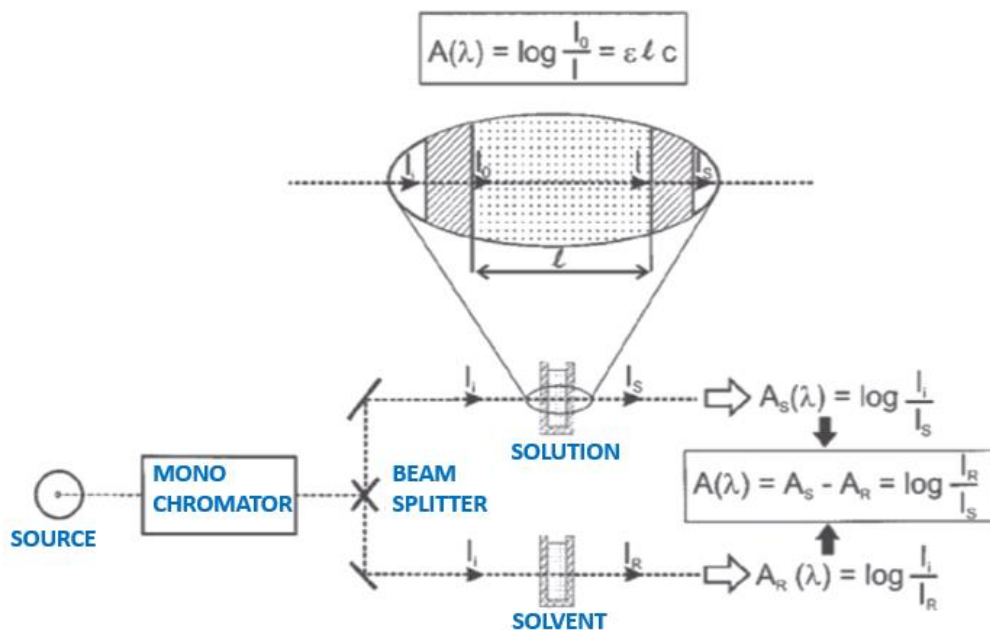
Figure 16. Absorbance measurement in a double-beam spectrophotometer.

### 2.1.4. Fluorescence Emission

Steady state fluorescence intensity $I_F(\lambda_F)$ as a function of fixed excitation wavelength, $\lambda_F$, is proportional to the photon's absorption intensity $I_A(\lambda_E)$ at the excitation wavelength $\lambda_E$. But also, proportional to the probability distribution function of the electronic relaxation from the singlet excited state (S1->S0), $F_\lambda(\lambda_F)$, through an instrumental constant $k$, dependent on the measurement geometry (collection angle), transmitting efficiency, monochromator width and the photomultiplier potential difference.[32][33]

$$I_F(\lambda_E, \lambda_F) = k\, F_\lambda(\lambda_F)\, I_A(\lambda_E) \qquad (16)$$

The photon's absorption intensity is given by the difference between the incident beam intensity, $I_0$, and the transmitted beam, $I_T$, at the excitation wavelength

$$I_A(\lambda_E) = I_0(\lambda_E) - I_T(\lambda_E) \qquad (17)$$

The light transmitted beam intensity is given using the Beer-Lambert law, by

$$I_T(\lambda_E) = I_0(\lambda_E)e^{-2,3\varepsilon(\lambda_E)lc} \qquad (18)$$

Where $\varepsilon(\lambda_E)$ is molar absorption coefficient at the excitation wavelength, $l$ is the optical path (cm), $c$ the molar concentration (mol L$^{-1}$), the portion $\varepsilon(\lambda_E)lc$ represents the absorbance at the excitation wavelength $A(\lambda_E)$.

Relating the above-mentioned equations, the following equation is obtained

$$I_F(\lambda_E, \lambda_F) = kF_\lambda(\lambda_F)I_0(\lambda_E)(1 - e^{-2,3\varepsilon(\lambda_E)lc}) \qquad (19)$$

The conventional spectrofluorometer, figure 17, consists in a light source, generally a high-pressure xenon arc lamp, that offers continuous emission from ~250 nm to infrared region. A monochromator is used to select the excitation wavelength. Fluorescence is collected at right angle with respect to the incident beam and detected through a monochromator by a photomultiplier. Automatic scanning of wavelengths is achieved by the motorized monochromators, which are controlled by the electronic devices and the computer (in which the data are stored).

The optical module contains the sample holder, shutters, polarizers, and a beam splitter consisting of a quartz plate reflecting a few percentages of the exciting light toward a quantum counter or a photodiode.
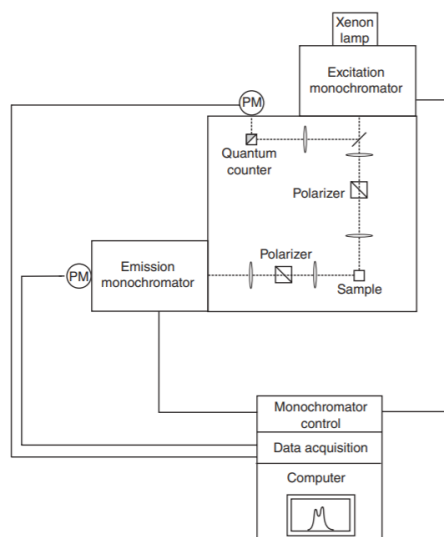
Figure 17. Conventional spectrofluorometer.

### 2.1.5. Förster Resonance Energy Transfer

Upon light absorption an electronically excited singlet state of a donor is generated, this state transfers energy through a long range single-step radiationless process to an acceptor chromophore, inducing the excited state of the acceptor, as the donor relaxes back to its ground state. Excitation energy transfer requires that the electronic interaction between donor and acceptor is strong enough so that the energy transfer is faster than the usual photophysical decay processes that depopulate the excited singlet states. Singlet-singlet energy transfer occurs mainly through dipole-dipole mechanism, the Förster type mechanism, requiring the spectral overlap of donor and acceptor as well as spatial proximity of both molecules. On the other hand there's no need for overlap electronic orbitals of both agents involved, as in the case of Dexter electron-exchange mechanism (shorter distances, strong coupling), more probable for triplet-triplet energy transfer.

The excitation energy transfer rate $k_{DA}$, for a weak donor-acceptor interaction (distances higher than 2 nm) is given by:

$$k_{DA} = \frac{2\pi}{\hbar} |V_{DA}|^2 J_{DA} \qquad (24)$$

Where $V_{DA}$ denotes the excitonic coupling between the energy donor and the receptor, and $J_{DA}$ the spectral overlap integral. If the distance between donor and acceptor is bigger than the size of both, the interaction is long-ranged. This Coulomb coupling can be expand into a multi-pole series of dipole-dipole terms, which consists in the Förster formula:

$$k_{DA} = \frac{9000(\ln 10)\kappa^2 \phi_D}{128\pi^5 n^4 N_A r^6 \tau_D} \int_0^\infty \frac{f_D(\tilde{v})\varepsilon_{DA}(\tilde{v})}{(\tilde{v})^4} \qquad (25)$$

Where $\kappa^2$ is an orientational fator dependent on the angles between D and A transition dipole moments, assumed to be 2/3 for random orientations; $r$ the distance between D and A, $\phi_D$ the fluorescence quantum yield, $\tau_D$ the excited lifetime of D in the absence of A; $N_A$ is the Avogadro

number, $f_D(\tilde{v})$ the normalized fluorescence intensity of D and $\varepsilon_{DA}(\tilde{v})$ the extinction coefficient of A at the wavenumber of transition, $\tilde{v}$. The refractive index of the medium is represented by $n$. The energy transfer rate depends inversely on the refractive index of the medium since the index of the pigments' local surroundings is of considerable importance for assessment of absolute rates.

Förster equation can be written in terms of the Förster critical transfer radius, $R_0$, the distance at which the transfer efficiency equals 50%.

$$k_{DA} = \frac{1}{\tau_D}\left(\frac{R_0}{r}\right)^6 \quad (26)$$

In turn, the efficiency of FRET is given by:

$$E = \frac{1}{1+\left(\frac{r}{R_0}\right)^6} \qquad (27)$$

FRET occurs for allowed singlet-singlet transitions if the emission of the energy from the electronically excited singlet state of the donor and the absorption of acceptor overlap significantly. For these kind of transitions the critical transfer radius vary within the range of 1 to 10 nm. Besides that, a favourable orientation of D and A transition dipole moments is needed in order to obtain an efficient FRET process, if the dipole moments are perpendicular to each other FRET doesn't occur. Although being vastly used to calculate distances at the nanoscale level; the distances range that can be probed b this technique is limited. The dependence on $\left(\frac{1}{R}\right)^6$ makes distances in the range of $0.5$-$1.5R_0$, corresponding to FRET $E$ between 0.98-0.10 are suitable for FRET measurements. At higher distances, the FRET efficiency drops to zero, at shorter distances, the value is close to one.[34]

### 2.1.6. Zeta potential

Zeta potential, figure 18, is a physical property which is exhibited by any particle in suspension, macromolecule or material surface, used as a key parameter to control surface charge of particles.

The liquid layer surrounding the particle exists as two parts; an inner region (Stern layer) where the ions are strongly bound and an outer (diffuse) region where they are less firmly associated. The diffuse layer features a notional boundary inside which the ions and particles form a stable entity. When a particle moves (e.g. due to gravity), ions within the boundary move with it. Those ions beyond the boundary stay with the bulk dispersant. The potential at this boundary is the zeta potential, ζ-potential.
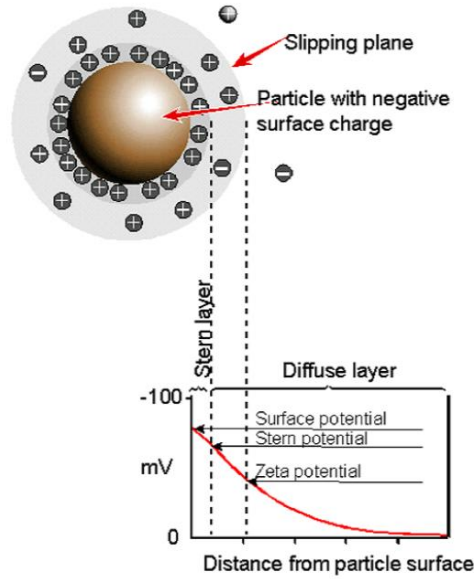
Figure 18. Schematic representation of the ζ-potential.

The magnitude of the zeta potential gives an indication of the potential stability of the colloidal system.

Through electrophoresis, when an electric field is applied across an electrolyte, charged particles suspended in the electrolyte are attracted towards the electrode of opposite charge. Viscous forces acting on the particles tend to oppose this movement. When equilibrium is reached between these two opposing forces, the particles move with constant velocity. The velocity of a particle in a unit electric field is referred to as its electrophoretic mobility.[35][36]

$$\mu_e = \frac{V}{E} \quad (20)$$

Where $V$ is the particle's velocity (μm/s) and $E$ the electric field strength (V/cm)

Zeta potential, $\zeta$ (mV or V), is related to the electrophoretic mobility by the Henry equation

$$\mu_e = \frac{2\,\varepsilon_r\,\varepsilon_0\,\zeta\,f(ka)}{3\eta} \qquad (21)$$

Where $\varepsilon_r$ is the dielectric constant of the dispersion medium, $\varepsilon_0$ is the permittivity of free space,

When the electrical double layer thickness is inferior to the particles radius, observed for large particles (>1μm) dispersed in high saline concentrated aqueous solutions (10⁻²M), $f(ka) = 1,5$, referred as Smoluchowski model

$$\mu_e = \frac{\varepsilon_r\,\varepsilon_0\,\zeta}{\eta} \qquad (22)$$

Otherwise, for small particles (≤100nm) dispersed in low saline concentrated aqueous solutions (10⁻⁵M), $f(ka) = 1$, referred as the Hückel model.

Electrophoretic light scattering, known as laser Doppler, figure 19, electrophoresis, or phase analysis light scattering (PALS) is a method for measuring electrophoretic mobility, and then calculating $\zeta$ potential. Laser Doppler electrophoresis measures small frequency shifts in the scattered light that arise owing to the movement of particles in an applied electric field. The frequency shift $\Delta f$ is equal to

$$\Delta f = \frac{2v\sin(\theta/2)}{\lambda} \quad (23)$$

Where $v$ is the particle velocity, $\lambda$ is the laser wavelength and $\theta$ the scattering angle ($\theta \sim 13°$).
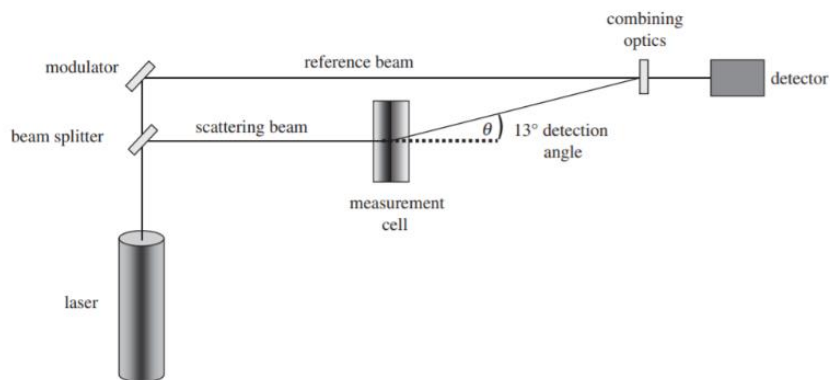


Figure 19. Laser Doppler electrophoresis instrument.

### 2.1.7. Fluorescence Microscopy

The fluorescence microscopy technique used in this Thesis was Fluorescence lifetime imaging microscopy (FLIM). The equipment operates in the time domain TCSPC and uses confocal detection. For the state of clarity the description of the principles involved in confocal microscopy will be separated from a further detailed description of FLIM technique

#### 2.1.7.1. Fluorescence lifetime imaging microscopy

Fluorescence lifetime imaging microscopy, FLIM, figure 20, is a technique where the contrast is based on the lifetime of individual fluorophores. As mentioned above, fluorescence lifetime is defined as the average time that a molecule remains in an excited state prior to returning to the ground state by emitting a photon. Since the lifetimes are highly sensitive to physical conditions in the local environment, such as temperature, pH, oxygen levels, polarity, binding to macromolecules and ion concentration, while being independent on concentration, absorption by the sample, sample thickness, photo-bleaching and/or excitation intensity, FLIM is considered to be an effective way to study dynamic processes, for instance in living cells. [32][37]
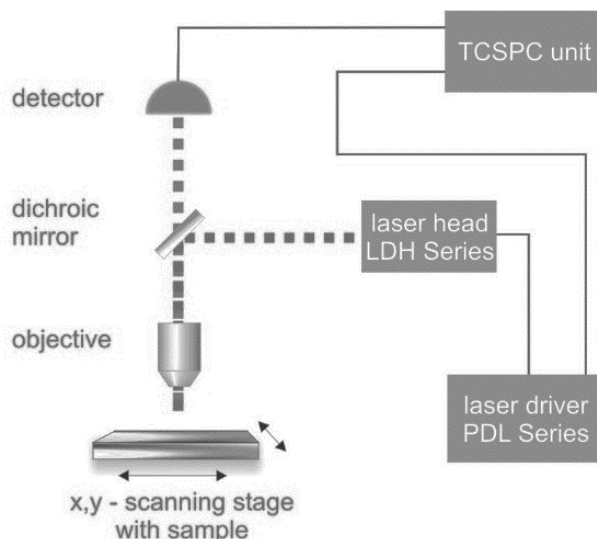
Figure 20. Typical set-up of a fluorescence lifetime imaging microscope.

Fluorescence lifetime-based imaging is widely used in the biomedical sciences, conjugated with Förster resonance energy transfer (FRET) to identify interactions or conformational changes.

### 2.1.7.2. Time-Correlated Single Photon Counting

Time-Correlated Single Photon Counting (TCSPC) is used to determine the fluorescence lifetime, the time between sample excitation by a pulsed laser and the arrival of the emitted single photon at the detector is measured. The measurement of this time delay is repeated many times to account for the statistical nature of the fluorophore's emission. The delay times are sorted into a histogram that plots the occurrence of emission over time after the excitation pulse. In order to acquire a fluorescence lifetime image, the photons must be attributed to different pixels, which is done by storing the absolute arrival times of the photons additionally to the relative arrival time in respect to the laser pulse. Line and frame marker signals from the scanner of the confocal microscope are additionally recorded in order to sort the time stream of photons into the different pixels.

### 2.1.8. Transmission Electron Microscopy

Transmission electron microscopy (TEM), is a powerful microscopy technique in which a beam of electrons offers a powerful tool to exam some fine features whose characteristic dimensions are less than 100 nm in size (or even down to atomic scale in some cases).

Electron beams, generated from an electron gun, could be closely focused by metal apertures and electromagnetic lens in the column of a TEM. The beam of highly energetic electrons is transmitted through the sample and the interactions that take place inside the irradiated sample affect the electron beam.

Some sample features have an impact on the transmission of the electron beam, such as the density or composition of the studied specimen. More electrons would pass through porous metal,

whereas less would pass for much denser materials. By applying a condenser lens in TEM, the crystal structure information of a specimen could also be acquired by the paralleled electrons beams.

The transmitted electrons are focused and then magnified by an electromagnetic lens system of two lenses after they pass through the specimen, being then projected on a phosphor screen to convert the electron image information to a visible form. In the entire imaging system, the emitting directions of electrons could be changed with electromagnetic lens such as condenser, objective, and projective lens.

Observation techniques performed in bright-field and dark-field mode are based on the transmitted and diffracted electrons, respectively. In the bright-field mode, only the transmitted electrons can pass through the aperture, the resulting image is based on the weakening of direct electron beam as it passes through the specimen. Thus, the thick area and inclusions of heavy atoms of the specimen show dark on the screen. Although, in the dark-field mode, the transmitted electrons are blocked by the aperture, the diffracted electrons can pass through it. As a result, the crystal information of a specimen could become bright to be viewed in dark-field mode if it could satisfy the corresponding diffraction condition.

The whole trajectory from source to screen is under vacuum, and the sample thinness should be guaranteed to allow the electrons to penetrate it. [38][39]

### 2.1.9. Confocal Microscopy

Confocal Microscopy is an optical imaging technique to obtain sharper, more detailed 2D images at different specimen's depths. Successive slices make up a 'z-stack', which can either be processed to create a 3D image.

Confocal microscopes, figure 21, use a focused spot of light to scan the specimen. The fluorescence emitted by the specimen is separated from the incident beam by a dichroic mirror and is focused by the objective lens through a pinhole aperture to a photomultiplier. Fluorescence from out-of-focus planes above and below the specimen strikes the wall of the aperture and cannot pass through the pinhole.[32]
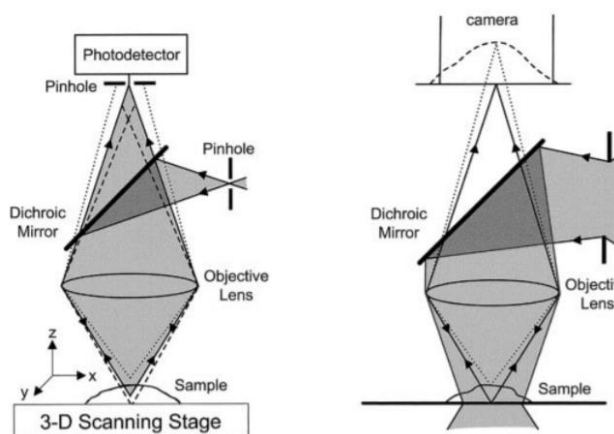
Figure 21. Principle of confocal microscopy (left) and conventional microscopy (right).

It should be noted that, because confocal microscopy collects only a fraction of the total fluorescence emitted by a sample, the excitation energy required to image this fluorescence must be higher than in conventional fluorescence microscopy. Therefore, the amount of photobleaching per detected photon is higher. This photodegradation phenomena should be minimized by using stable fluorophores and by operating the confocal microscope at low laser power, high detector sensitivity, and maximum objective numerical aperture.

## 2.2. EXPERIMENTAL PROCEDURES
### 2.2.1. Materials

Poly(sodium 4-styrenesulfonate) [PSS (MW~75000, 18% wt % in water)] and poly(allylamine hydrochloride) [PAH (MW~17500)], obtained from Sigma-Aldrich. Sodium chloride [NaCl (MW~58,44, ≥99,5% purity)], obtained from Fisher Chemical. Sodium carbonate [$Na_2CO_3$ (MW~105,99)] obtained from J. T Baker. Calcium chloride [$CaCl_2$ (MW~147,02)] obtained from Merck. Sodium Hidroxide [NaOH (MW~40,00)], chloride acid [HCl (7%)] obtained from Sigma Aldrich for pH ajusts. Meso-(tetrakis)-(p-sulfonatophenyl) porphyrin [TSPP (MW~1022,908)] was obtained from Fluka (≥98% purity), Rhodamine 6 G, [R6G (MW~443,564)]) was obtained from Radiant Dyes & Accessories, and Sodium dihydrogen phosphate monohydrate [$NaH_2PO_4.H_2O$ (MW~137,99)] obtained from Riedel-de-Haen.

Polyelectrolyte solutions PSS (3 mg/mL, 0,5M NaCl), and PAH (13 mg/mL, 0,5 M NaCl) were prepared in bi-distilled $H_2O$, and the pH was adjusted to 6.4 (for PSS/PAH polyelectrolyte microcapsule preparation). Porphyrin solution TSPP (1,25 mg/L) pH was adjusted to 8 with NaOH addition, and rhodamine R6G solution (125µM) was prepared with no pH adjust since the specie nature doesn't change with pH. The salt solution $NaH_2PO_4.H_2O$ 0,68% (w/v), pH=7,2 was prepared for the release studies.

#### 2.2.1.1. Preparation of the $CaCO_3$ templates

$CaCO_3$ colloidal templates were prepared by co-precipitation of $CaCl_2$ (0,33M, 1mL) and same volume solution of $Na_2CO_3$ (33M, 967µL) with PSS (6,6 g/L, 33 µL), under vigorous stirring for 30 seconds. The suspension was left during 15 minutes at room temperature. The $CaCO_3$ templates were recovered after supernatant removal by three washing/ centrifugation cycles with bi-distilled $H_2O$ (3000 rpm, 2min). [40]

#### 2.2.1.2. Polyelectrolyte layer-by-layer assembly- PE shell assembly

The $CaCO_3$ microparticles were dispersed in aqueous solution of polyelectrolyte (1mL, $C_{PSS}$=3mg/mL, $C_{PAH}$=13mg/mL, 0,5M NaCl, pH 6,4). After stirring for 20 minutes, the resulting particles were recovered by three washing/ centrifugation cycles with bi-distilled $H_2O$ (3000 rpm, 2 min), to remove residual polyelectrolyte. Between the centrifugation cycles vortex and ultrasounds were applied, so that $CaCO_3$ particles would be suspended in the bi-distilled washing $H_2O$. The assembly's order of each polyelectrolyte layer varied according to the system architecture. The alternate adsorption of the oppositely charged PEs started always with the negative PE PSS. To guaranty the potential stability of the colloidal system, measured by the zeta-potential the first layer of PAH consists of three additions of PAH; furthermore, three washing/ centrifugation cycles with bi-distilled $H_2O$ was performed for 15 minutes, 6000 rpm.

#### 2.2.1.3. Porphyrin adsorption onto PE MCs

TSPP was adsorbed onto the PE shell with PAH as the last layer. The polyelectrolyte shell microcapsules were suspended in a TTSPP solution (0,25mg/L) pH 8, and the system was left

stirring for 1,5 hours at room temperature. Afterwards, three cycles of washing/centrifugation (3000 rpm, 2 min) were performed with bi-distilled $H_2O$, to recover the porphyrin-polyelectrolyte shell cores and discard non-adsorbed porphyrin, and free polyelectrolyte molecules in the solution.

### 2.2.1.4. Rhodamine adsorption onto PE MCs

R6G was adsorbed onto the PE shell with PSS as the last layer, suspending the microcapsules in a solution 0.046mM R6G and 1.2mg/mL of PSS. The polyelectrolyte shell microcapsules were suspended in the R6G solution, the system was left stirring for 1.5 hours at room temperature. To remove free non-adsorbed rhodamine and free polyelectrolyte molecules in the solution, three washing/centrifugation cycles (3000 rpm, 2 min) were performed with bi-distilled $H_2O$.

### 2.2.1.5. Polyelectrolyte microcapsules porphyrin and rhodamine release

Microcapsules with both porphyrin and rhodamine adsorbed in distinct PE layers suspended in a release solution, salt solution $NaH_2PO_4.H_2O$ 0,68% (w/v) physiological pH=7,2, under stirring. Released porphyrin and rhodamine are recovered over time by collecting the supernatant after centrifugation (3000 rpm, 4 min). The medium is renovated after each sample collection.

### 2.2.2. Equipment

Steady-state UV-Visible absorption spectra were recorded in a Perkin-Elmer Lambda 35 UV/Vis spectrophotometer. Quartz cells with an optical path length of 1 cm were used. Steady-state fluorescence emission and excitation spectra were measured with a Fluorolog FL-1040 Horiba Jobin Yvon with a 450 W xenon lamp.

Zeta-potentials measurements were performed in a Zetasizer Nano ZS equipment obtained from Malvern Instruments Ltd and using Zetasizer nano-ZS software.

The pH adjustments were done with pH sensor Denver Instrument Model 15 and the pH electrode Mettler Toledo AG 30281915 Rev A.

TEM images were obtained with Hitachi H-8100 electron microscope operated at 200 kV, with an energy dispersive X-ray spectrophometer (EDS).

FLIM measurements were performed with a MicroTime 200, from PicoQuant (Germany), equipped with an Olympus IX-71 microscope. Data acquisition is performed with SymPho Time Software 5.3.2.2. version. Fluorescence excitation, at the wavelengths 482 and 638nm, was performed with two different pulsed picosecond diode lasers, the pulse repetition rates were 20 MHz and 10 MHz, in case of R6G and of TSPP, respectively. The laser pulsed light goes to the main optical unit through an optical fiber, it traverses collimating lens, a bandpass filter, and a mirror before reaching the excitation shutter. During this path the beam is filtered and 90 ˚deviated from its initial direction, its polarization is horizontal relatively to the main optical unit, which also lies horizontally. Approximately half of the beam intensity is then reflected by a beam splitter, to the photodiode which measures the actual excitation intensity. The read-out is given in arbitrary

units and requires a calibration curve for each laser head. The major dichroic directs the excitation beam to the right-side port of the microscope, through an adjustable beam displacer unit that compensates for minor misalignments between the microscope and the main optical unit. The beam then enters the microscope and it is focused on the sample through the objective. Sample's emission as well as some backscattered light goes through the reverse pathway passing the major dichroic mirror, and then a filter. The bandpass filter with a bandwidth of 55 nm, centred at 695 nm (695AF55 Omega Optical) was used for de laser 638 nm, and a long-pass filter (510ALP, Omega Optical) that blocks light below 510 nm was used with the 482nm diode laser. A pinhole of 50 um was always used to reject out of focus light. Two detectors, SPAD detectors (SPCM, AQR-13, Perkin Elmer) detect the system's fluorescence. For the TCSPC data acquisition a Time-Harp 200 TCSPC PC-board from PicoQuant is used working in the special time-tagged time-resolved (TTTR) mode. The objective Olympus 60x, NA 1.2, water-immersion combined with Olympus IX-71 microscope can be moved in the X-Y plane with a E-710 Digital PZT Controller, from Physik Instrumente. Emission spectra were obtained using a coupled spectrometer QE Pro, Ocean Optics.

## 3. RESULTS AND DISCUSSION

The TSPP and R6G behaviour with polyelectrolytes, PSS and PAH in aqueous solution was studied prior to their assembly in the MCs. After the PE aqueous solution studies, the next procedure was the design an assembly of the MCs. In the end of this experimental work, the release study of TSPP adsorbed in MCs, at pH 7.2 media.

### 3.1. Porphyrin interaction with Polyelectrolytes in aqueous solution

Porphyrins have a natural tendency to self-assemble through π- π stacking and other weak intermolecular interactions. This feature results in nanometric structures with interesting optical and electronic properties, distinct from those of the monomer. Since the aim of this Thesis is to study functionalized microcapsules prepared with polyelectrolytes, PAH and PSS, the behaviour of porphyrin in aqueous solution with both PE should be taken as reference.

The aggregation of the anionic porphyrin meso-tetrakis(p-sulfonatophenyl)porphyrin sodium salt, TSPP, has been studied extensively. Under proper conditions, involving very acidic media and high ionic strength, TSPP forms highly ordered molecular J and H aggregates [41][42][43].The main requisite to form J-aggregates is the zwitterionic character with protonation of the pyrrole nitrogen in the macrocycle. These aggregates have been reported also by interations between the porphyrin and surfactants [44][45].

At pH 7, figure 22, to avoid its diacid form, the aqueous soluble porphyrin features its Soret band at 413 nm, and the Q bands: $Qy(1,0)$ at 516 nm, $Qy(0,0)$ at 553 nm, $Qx(1,0)$ at 579 nm and $Qx(0,0)$ at 633 nm. The emission maxima features two peaks at 645 nm and 706 nm ($\lambda_{exc}$=483 nm).
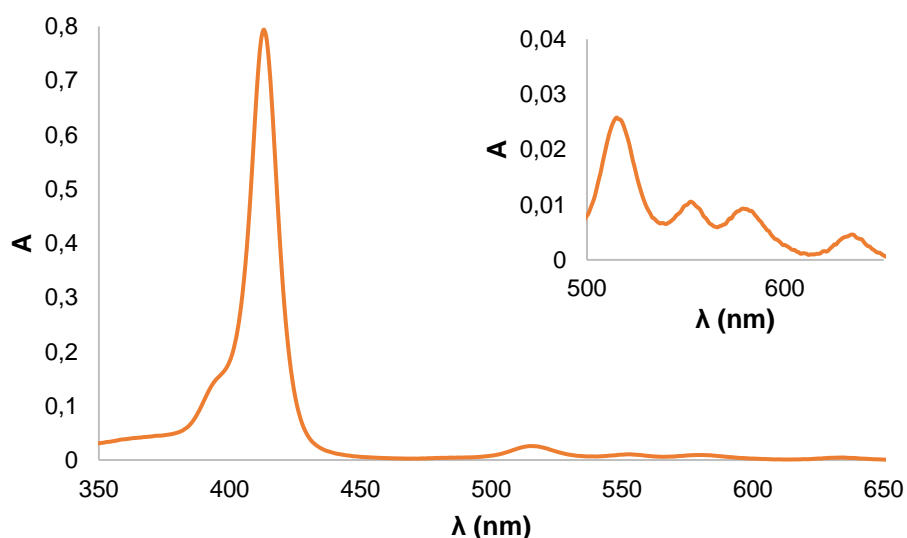


Figure 22. UV-Vis absorbance spectra of TSPP (1.6μM, pH 7, water). The inset shows the corresponding Q-bands.

### 3.1.1. TSPP and PAH interaction

The titration of TSPP at a fixed concentration (2 μM) with variable amounts of PAH was followed by absorption, and fluorescence at pH 7, figure 23 and figure 24, respectively. The interaction of TSPP with PAH results in the formation of H-aggregates, as shown by the blue-shifted Soret peak at 401 nm in the respective absorption spectrum. TSPP spectral features are maintained within a range of PAH concentrations, changing after an added concentration of 20μM of PAH. On the other hand, the Q-bands suffer a red-shift, from 516 nm to 525 nm for the Qy(1,0) band, 553 nm to 561 nm for the Qy(0,0) band, 579 nm to 600 nm for the Qx(1,0) band and finally 633 nm to 655 nm for the Qx(0,0) band. When the TSPP monomers stack parallelly, form H-aggregates resulting on the typical detected blue-shift. Similar aggregation phenomenon causing a blue shift were observed for TSPP in association with the polyelectrolyte polybrene at neutral pH. [46][47][48]
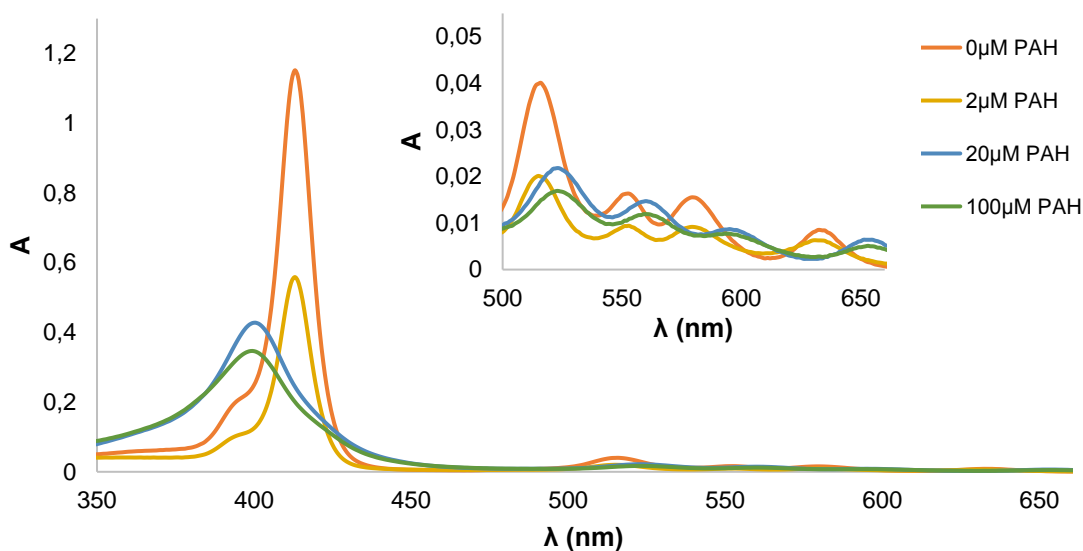


Figure 23. UV-Vis absorbance spectra of TSPP (2μM, pH 7, water) in the presence of increasing concentrations of PAH. The inset shows the corresponding Q-bands.

The emission spectrum below (figure 24) shows a pronounced red-shift moving from 644nm and 704 nm, in water, to 665 nm and 727nm, in PAH (20μM) aqueous solution, together with a significant decrease of the fluorescence intensity. It is plausible that the positive amine groups of PAH induce the aggregation of TSPP and, because of this, the emission is quenched, when compared with emission in aqueous solution. The electrostatic force between the oppositely charged sulfonate and amine groups should not be the unique force involved in the complexation of TSPP in aqueous PAH. There must be a balance between electrostatic and hydrophobic forces (π-π stacking) bringing the porphyrins closer to each other, arranged in a cofacial dimer.
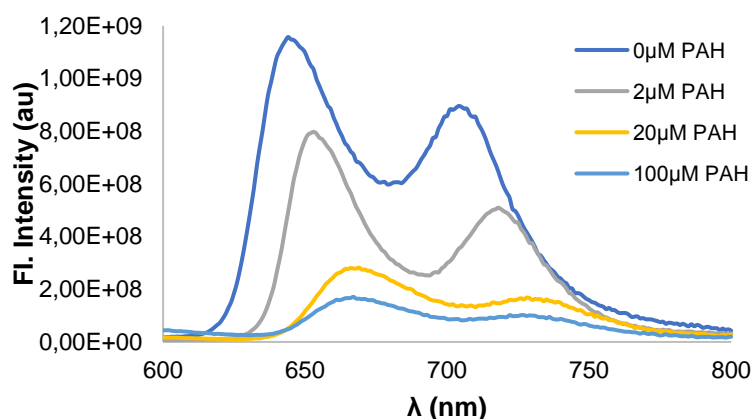
Figure 24. Fluorescence emission spectra of TSPP, (2µM, pH 7, water) in the presence of increasing concentrations of PAH, $\lambda_{exc}$=483 nm.

### 3.1.2. TSPP and PSS interaction

Incubation of TSPP monomers with negatively charged polyelectrolyte PSS resulted in no colour change of the porphyrin solution. The UV-Vis absorbance and emission spectra of TSPP pH 7 in the presence of increasing concentrations of PSS shown no shifts of the maximum bands, only an increase of the both signals with the increase of added PSS, figure 25 (A) and (B). This increase could be accounted by a possible disaggregation of TSPP existing in solution which would lead to a wider less intense Soret band and fluorescence quenching. However, comparing with already existing literature data [50] there is no evidence of such enlargement nor is the fluorescence quantum yield decreased ($\phi_f$~0.1). Another hypothesis would be a change in the surrounding environment of TSPP molecules caused by the interactions with PSS chain groups.
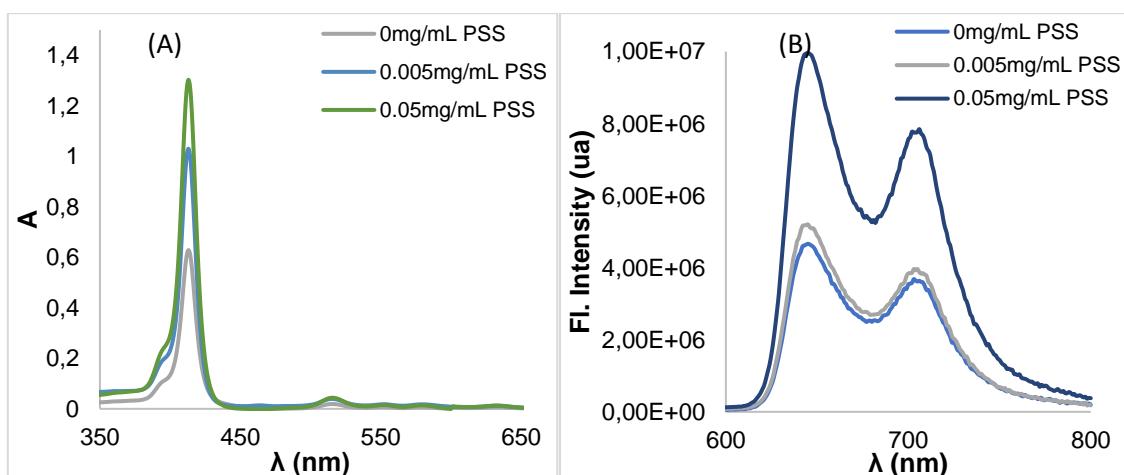


Figure 25 (A) UV-vis absorbance spectra of TSPP (1.2 µM, pH 7, water) in the presence of increasing concentrations of PSS; (B) Fluorescence emission spectra in the presence of increasing concentrations of PSS, $\lambda_{exc}$=483 nm.

### 3.1.3. TSPP and both PAH and PSS interaction

The competition between TSPP and PSS for the opposite positively charged electrolyte PAH was also studied, varying the addition order of PSS and PAH. Firstly, this interaction was carried out by adding PSS (concentrations range from 0, 2, 20 and 100 µM) to TSPP (1.2 µM), and then the

last addition was an aliquot of PAH (2 μM), figure 26. For the 0μM PSS addition, the equimolar combination of TSPP and PAH displays no variation of the Soret band, and agrees with the previous study of TSPP and PAH interaction; the addition of 2 μM of PSS, causes a red shift of the Soret band from 413 nm to 425 nm. When it comes to the addition of 20μM PSS, the Soret peak appears at 413 nm, seems like the monomeric form of TSPP is predominant, and there's a shoulder which might be linked with monomeric TSPP interacting with PAH-PSS conjugate For the maximum concentration of added PSS, 100 μM, there's a red shift of 10 nm, resulting in the appearance of the Soret band at 423 nm, which might be linked to tetranions of TSPP aggregating with themselves, induced by the proximity of TSPP to PAH in a PAH-PSS conjugate.
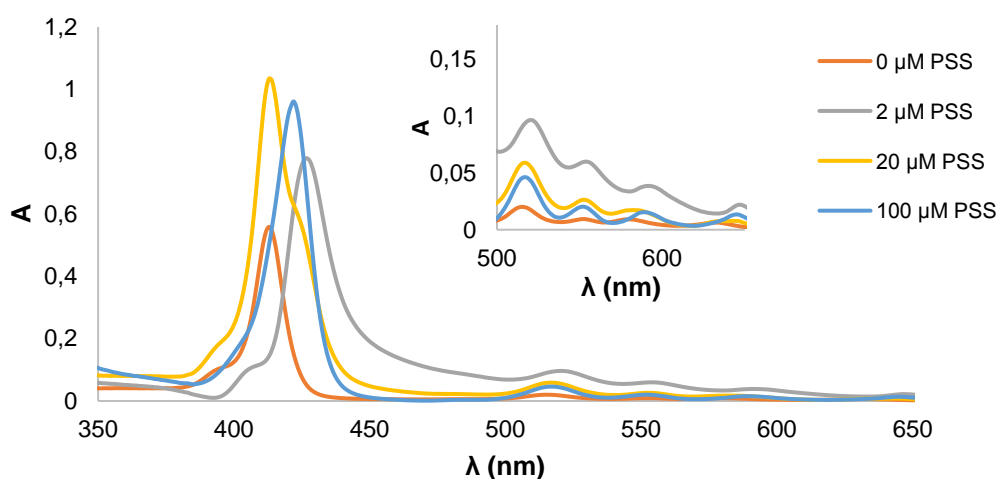


Figure 26. UV-Vis absorbance spectra of TSPP (1.2μM) and PAH (2μM), with increasing concentrations of PSS. The inset shows the corresponding Q-bands.

The emission spectrum, figure 27, shows a blue-shift moving from 656 nm and 721 nm, to 650 nm and 715 nm, and the emission quenching when PSS is added to the aqueous solution.
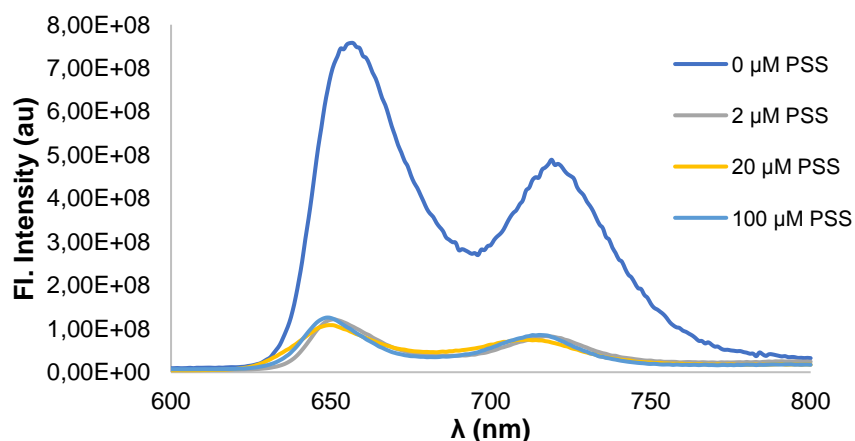


Figure 27. Fluorescence emission spectra of TSPP (1.2μM), increasing concentrations of PSS, and and PAH (2μM). $\lambda_{exc}$=483 nm.

Then, aiming to study the importance of the adding order of the positively charged polyelectrolyte, PAH, the same study was carried but this time adding the variable concentration of PSS as the last step. No major spectral feature had changed.

TSPP and PAH interact since the positive PE with its positive amine groups induces the H-aggregation of the porphyrin. However, with the addition of the opposite charged PE, PSS, it is likely that the PAH molecules have affinity for it, causing some disaggregation of the previously formed porphyrin H-aggregates.

Discrete lifetimes provided by multi-exponential analysis are normally regarded as model to compare if the porphyrin is aggregated if it is quenched by the surrounding molecules or if the polarity of the environment changed (table 2). The monoexponential decay yielding a lifetime of 10 ns agrees well with other published results and show that TSPP is in its monomeric form at the chosen conditions of pH and concentration in water [48]. The decay measured in PAH 20µM aqueous solution resulted in the emergence of a discrete lifetime of 2.6ns, already reported by others and justified as a population of H-aggregates [41]. For the decay in PAH/PSS (1:1) there is a distribution of two populations, with a discrete lifetime of 4.8 ns, and 10 ns; the first one might be assigned to the interaction of tetranions of TSPP monomers with PAH, and also on TSPP being sandwiched between PAH and PSS molecules, the second one, prevalent (59%) may be assigned to the porphyrin in its monomeric form.

Table 2. Fluorescence lifetimes of TSPP in aqueous solutions at pH=7.0 ($\lambda_{exc}$=483 nm, $\lambda_{em=}$ 650 nm).

|  | $\tau_1$ (ns) | $A_1$(%) | $\tau_2$ (ns) | $A_2$(%) | $\tau_3$ | $A_3$(%) | $\tau_{avg}$ | $\chi^2$ |
|---|---|---|---|---|---|---|---|---|
| Water | 10 | 100 | - | - | - | - | 10 | 1.066 |
| PAH* | 2.6 | 46.5 | 10.5 | 53.5 | - | - | 9.1 | 1.323 |
| PAH/PSS** | 4.8 | 41 | 10.6 | 59 | - | - | 9.2 | 1.193 |

*[PAH]=20µM; **[PAH]=2µM, [PSS]=2µM.

### 3.2. Rhodamine and Polyelectrolyte interaction

The visible absorption spectrum of R6G in aqueous solution is a function of dye concentration, pH and temperature. When very acid solutions are used (pH<2) the absorptivity in the visible region of spectrum decreases. This can be attributed to the lactonic structure (colourless) resulting from its Newman hydrolysis. The addition of NaOH decreases the fluorescence emission. When the dye concentration increases the absorption spectrum of R6G changes due to dimer formation ($M + M \rightleftharpoons D$). The dimer of R6G in aqueous solution adopts a sandwich structure where the planar xanthene groups of monomeric units are disposed in a parallel manner and a rotated angle. The hydrophobic character of substituents of rhodamines favours the parallel plane disposition of monomers in the aggregate to avoid water molecules. It seems that hydrogen bonds between monomer units and less-temperature dependent van der Waals forces are implied the parallel plane disposition of the chromophoric π-systems. [51]

The maximum absorption for R6G in aqueous solution is observed at 526 nm ($\varepsilon$ = 100000 M$^{-1}$cm$^{-1}$) for the monomer and at 498 nm for the dimer, also called H-dimer [51]. The weak shoulder at 500 nm in the monomer absorption is ascribed to a vibronic transition of the monomer band and a low H-content. Different concentrations of PSS were added to a solution of 0.35 µM R6G.

### 3.2.1. R6G interaction with PSS

The case of PSS-R6G mixtures is an example of specific polymer-dye interaction. Monomer dye interacting with PSS leads to a red-shift of the absorption band, with absorbance maximum at 534 nm. This strong hydrophobic interaction between PSS and R6G weakens the stacking interaction between bound dye cations. It is interesting to note that no clear dimer or aggregate band of R6G appears in PSS solution. In the inset of the figure 28, one can detect the minimum for monomer and dimer OD ratio corresponds to the first addition of PSS, which specify a strong increase of the R6G dimer relatively to the monomeric form. This PSS effect disappears with the increasing concentrations of the added PSS (the ODs ratio increases, and the Fluorescence Intensity/ OD max as well figure 28 inset, and figure 29 inset respectively). In the presence of a large excess of PSS, the dye is randomly distributed on the polymeric binding sites so that ion pairs are far away from each other, preventing their aggregation, where the spectrum of monomeric R6G is found red shifted. Thus, this polymer exhibits a high dispersant ability of this dye. In the case of PSS, the dimer/monomer ratio decreases as the PSS exceeds a certain minimum excess, and the fluorescence of the solution increases as the dye disaggregates.[51]
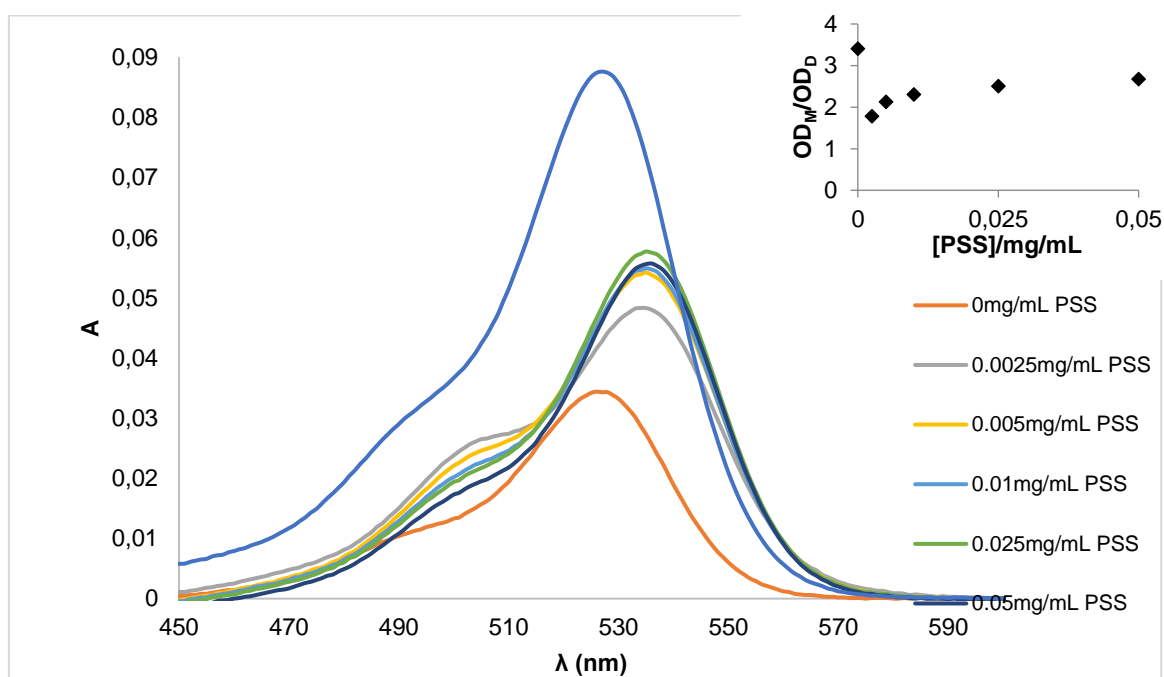


Figure 28. UV-Vis absorbance spectra of R6G (0.35µM) and increasing concentrations of PSS. OD$_{monomer}$ and OD$_{dimer}$ ratio versus the added concentration of PSS (mg/mL), inset.
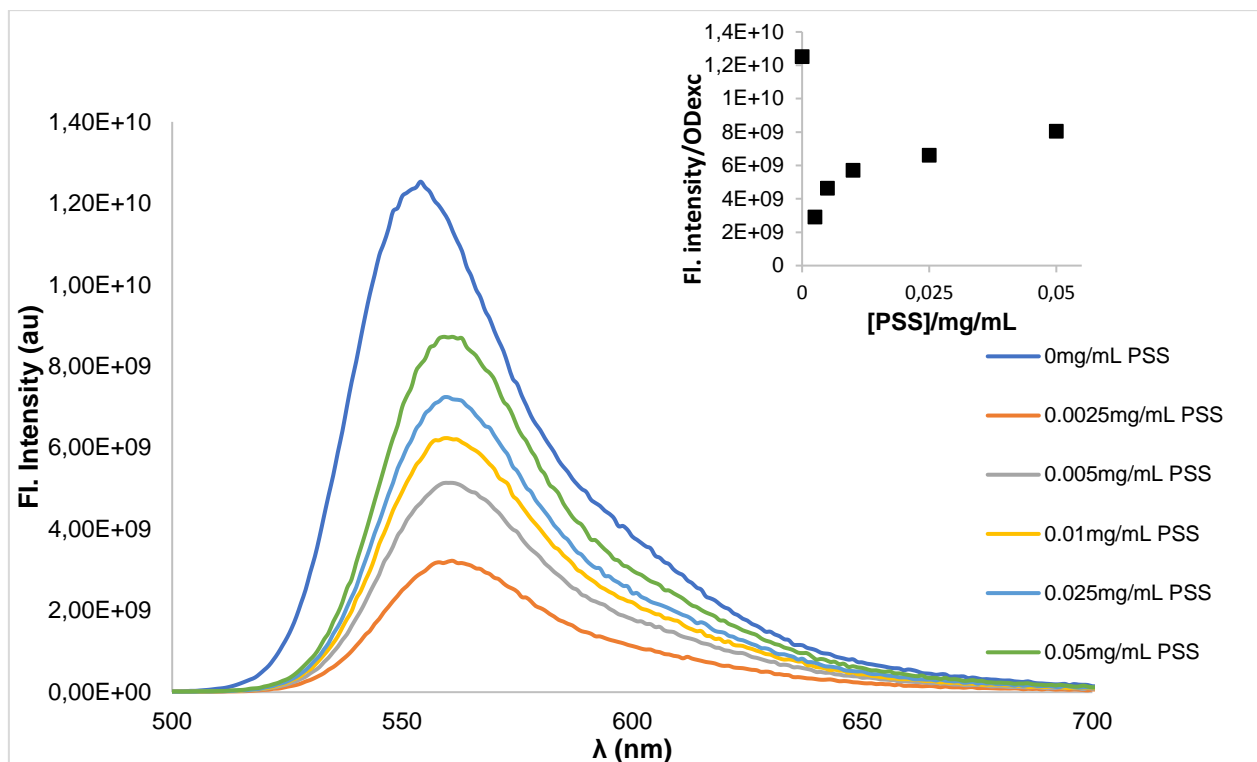
Figure 29. Fluorescence emission spectra of R6G (0.35µM) and increasing concentrations of PSS. $\lambda_{exc}$=483 nm. Intensity of fluorescence and $OD_{max}$ ratio versus the added concentration of PSS (mg/mL), inset.

### 3.2.2. R6G and both PSS and PAH interaction

In order to probe and compare the force of R6G-PSS and PAH-PSS interaction, PAH aliquots were added to a 0.45µM R6G, 5 µM PSS solution (0,056 mg/mL), figure 30. The importance of the addition order of the polyelectrolytes was also studied, when PSS was added as last step the following absorbance spectra was obtained figure 30 inset.

Evaluating the evolution of the spectra upon addition of increasing concentrations of PAH to the solution of R6G-PSS, there is a tendency to return to the free-rhodamine-like spectra. It seems that the equilibrium in the interaction between R6G, PSS, and PAH is shifted towards the formation of the polyelectrolyte complex PSS-PAH. Therefore, R6G cannot compete with the PAH-PSS complex at high amounts of polyelectrolytes. The PSS addition causes a red-shift on the free rhodamine peak, but when PAH is added as well there's a return to the initial *526 nm.* This gives us the possibility to use R6G as a marker for staining of PSS inside the PSS/PAH multilayers, without compromising the integrity of the future matrix of PE for the microcapsules. The study of the interaction between R6G and the positive polyelectrolyte PAH was carried and, as expected, it showed no interaction between dye and positive PE, since both are positively charged. When it comes to evaluate the impact of the addition order, it is possible to assure that the addition of PSS to R6G causes the red-shift on the R6G peak, returning to the maximum absorption for monomeric R6G after the PAH additions. For higher ratios of PAH/PSS (higher or equal to 1:1) the spectral features don't depend on the addition order. The competition effect is the PE affinity, PSS - PAH.
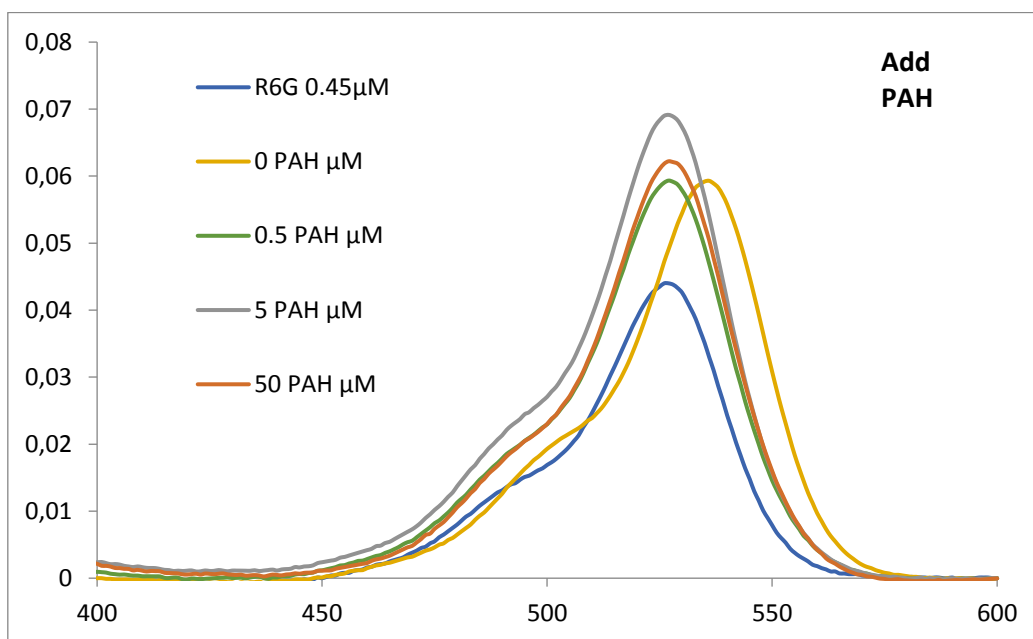
Figure 30. (A) UV-vis spectra of R6G (0.45μM), constant concentration of PSS (5μM) and increasing concentrations of PAH. (B) Inset of the same system but adding PSS (5μM) as final step. $\lambda_{exc}$=483 nm.

The fluorescence decay of R6G (table 3) in water is explained in literature as a monoexponential decay with a lifetime of about 3.8ns and 4.8 ns in a nonpolar solvent, although the best fitting was found to be a two discrete lifetime model, the discrete lifetime of 4.0 ns in water fits well with the published results. Although, the presence of dimers and/or aggregates tends to decrease the fluorescence lifetime (1.0 ns discrete lifetime component observed in water) due to the increase in the nonradiative pathways, occasioned by the coupling between the molecules, there's a coexistence of both dimer and monomeric forms, with a prevalency of monomers (88%) at 0.35μM R6G pH=7. In PSS aqueous solutions, there's a two discrete lifetime model fit of the fluorescence lifetimes, the 4.9 ns rhodamine lifetime increase should be due to the strong hydrophobic interaction between PSS and R6G, explained before. The discrete lifetime of 2.4 ns might be assigned to the interaction of a R6G aggregate with PSS. In solution with both polyelectrolytes there is a distribution of a monoexponential decay, with discrete lifetime 3.95 which might assigned to the R6G monomeric form, since it's near the monoexponential decay value of R6G in water, 3.8 ns. This is a strong evidence that PSS wins the competition for PAH, when R6G is, as well, in solution.

Table 3. Fluorescence lifetimes of R6G in aqueous solutions at pH=7.0. ($\lambda_{exc}$=483 nm, $\lambda_{em}$= 560 nm).

|  | $\tau_1$ | $A_1(\%)$ | $\tau_2$ | $A_2(\%)$ | $\tau_3$ | $A_3(\%)$ | $\tau_{avg}$ | $\chi^2$ |
|---|---|---|---|---|---|---|---|---|
| Water | 1.0 | 12.2 | 4.0 | 87.8 | - | - | 3.5 | 1.040 |
| PSS* | 2.4 | 15.5 | 4.9 | 84.5 | - | - | 4.4 | 1.043 |

| | | | | | | | | |
|---|---|---|---|---|---|---|---|---|
| PSS/PAH** | 4 | 100 | - | - | - | - | 3.95 | 1.022 |

*[PSS]=0.05g/L ; **[PSS]=5µM, [PAH]=5µM.

Due to the presence of PSS, fluorescence lifetime of R6G is higher when compared to free rhodamine in solution. The presence of PAH induces the diminishing of R6G fluorescence lifetime, since the PAH molecules compete for the PSS interaction.

### 3.3. TSPP and R6G interaction with both PSS and PAH in solution

In aqueous solution, the interaction between porphyrin, rhodamine and equimolar additions of (1:1, PAH:PSS) polyelectrolytes was studied figure 31. Apparently, when only TSPP and R6G are in solution no difference for the TSPP peak is shown, it maintains its maximum at 413 nm, on the other hand the rhodamine 6G peak is at 526nm. When the lower concentration of PAH/PSS (0.2 µM) is added no shift is detected on the Soret band of the porphyrin, but some loss of absorbance signal might be explained by the interaction of the porphyrin with PAH-PSS aggregate. For the 20µM equimolar PE addition, the Soret band suffers a red-shift to 423 nm, assigned to the disaggregate effect of PSS, wich interacts with PAH, resulting on the disassembly of porphyrin H-aggregates. Likewise, it seems that the competition for PAH is stronger for the opposite charged polyelectrolyte PSS, and TSPP is weaker in this case.
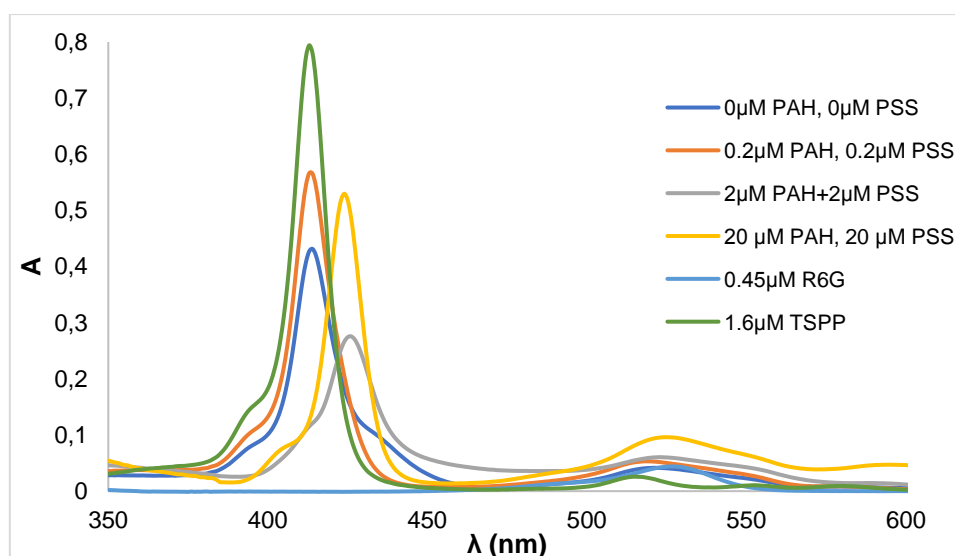


Figure 31. UV-Vis absorbance spectra of TSPP (0.85µM), R6G (0.43µM), increasing equimolar concentrations of PAH and PSS. The porphyrin/rhodamine sample with absence of polyelectrolytes isn't in its tetraanionic form (pH<7).
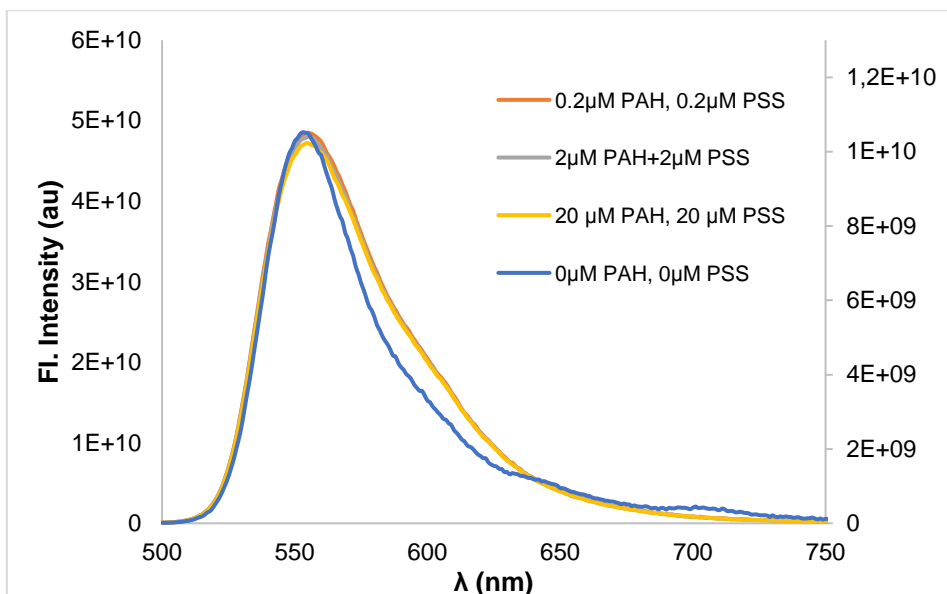
Figure 32. Fluorescence emission spectra of R6G, TSPP, increasing equimolar concentrations of PAH and PSS, the TSPP-R6G solution is analysed through the secondary axis. $\lambda_{exc}$=483 nm.

The rhodamine spectra show

a red-shift when PSS-PAH is added, which manifest some R6G interaction PSS-PAH conjugates, when TSPP is as well in the solution (figure 32). As one may notice, in the polyelectrolyte absence, TSPP-R6G display low fluorescence intensity signal. This data might be related with energy transference phenomena occurring favourably in the presence of PE, which might orientate de dipoles of both R6G and TSPP in a way excitation energy transference after excitation of R6G occurs, resulting in an enhanced fluorescence signal. The lifetime decay (table 4) shown a medium discrete lifetime of about ~3.97 ns for the R6G/TSPP in the absence of PE, which is not enough to support the occurrence of a excitation energy transference from R6G to TSPP (the R6G medium lifetime would have to be shorter to corroborate the hypothesis).

With this excitation wavelength the R6G emission peak was detected, and the addition of PSS increases the rhodamine signal. PSS and PAH interaction induce the absence of fluorescence intensity signal of the TSPP, which may be linked to the fact that PSS is less available to the porphyrin. The donor-aceptor Förster type interaction is compromised, since there's no energy transference the acceptor spectra is not visible and the donor spectra increases for the same reason. The intensity maintains since the polyelectrolytes, PSS and PAH, were being added with increasing concentrations equimolarly, which means, the amount of molecules of polyelectrolytes available will interact with themselves, resulting in less molecules but still some PSS accessible for R6G to interact with.

Table 4. Fluorescence lifetimes of R6G and TSPP in aqueous solution with polyelectrolytes, $\lambda_{exc}$=483 nm; $\lambda_{em=}$ 560 nm and $\lambda_{em=}$ 650 nm.

| | $\tau_1$ | $A_1(\%)$ | $\tau_2$ | $A_2(\%)$ | $\tau_3$ | $A_3(\%)$ | $\tau_{avg}$ | $\chi^2$ |
|---|---|---|---|---|---|---|---|---|
| PSS/PAH* | 0.34 | 56 | 3.9 | 44 | - | - | 3.42 | 0.977 |

| PSS/PAH** | 4.3 | 17 | 10.3 | 83 | - | - | 9.28 | 1.143 |
|---|---|---|---|---|---|---|---|---|

*[PSS], [PAH]=2µM; $\lambda_{em=}$ 560 nm; **[PSS], [PAH]=2µM $\lambda_{em=}$ 650 nm.

### 3.3.1. Imaging of the interaction of TSPP and R6G with both polyelectrolytes, PAH and PSS

A drop of the R6G/polyelectrolyte aqueous solutions was put in a glass slide and an image was obtained and resolved in terms of fluorescence lifetime and intensity. The diode laser was chosen to keep the same excitation used in cuvette measurements (483 nm) and the fluorescence signal was obtained for the all range of emissions (above 510 nm, using a long-pass filter). The images obtained for the rhodamine systems figure 33. These show some heterogenity when rhodamine and polyelectrolytes are free in solution and prevalence of green spots for the R6G/PSS/PAH system. The colour scale infers for the average lifetime of ~4 ns for this last system, which agrees well with the average fluorescence lifetime histogram distribution associated with this image also near 4 ns, and with the described lifetime of monomeric R6G ~3.8ns in water. In fact, as have been seen before, the interaction between R6G, PSS, and PAH seems to be shifted towards the formation of the polyelectrolyte complex PSS-PAH. Therefore, due to PE affinity, PSS – PAH, the population of free-rhodamine vs aggregated is higher. Observing the histogram curve of the system R6G/PSS which lifetime is about ~5ns, one can relate with the previous results which pointed to the presence of R6G bound randomly through the polymeric binding sites of PSS, the lifetime increase should be due to the strong hydrophobic interaction between PSS and R6G and agrees well with the lifetime obtained before (4.9 ns).
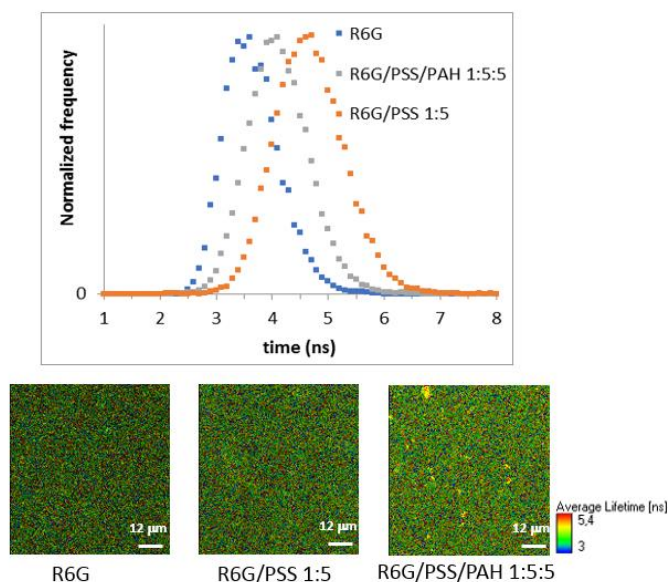


Figure 33. Fluorescence lifetime histogram of R6G in water, with PSS and with both polyelectrolytes, PSS and PAH. FLIM images, (A) R6G in water; (B) R6G/PSS 1:5 and (C) R6G with both PE 1:5:5.
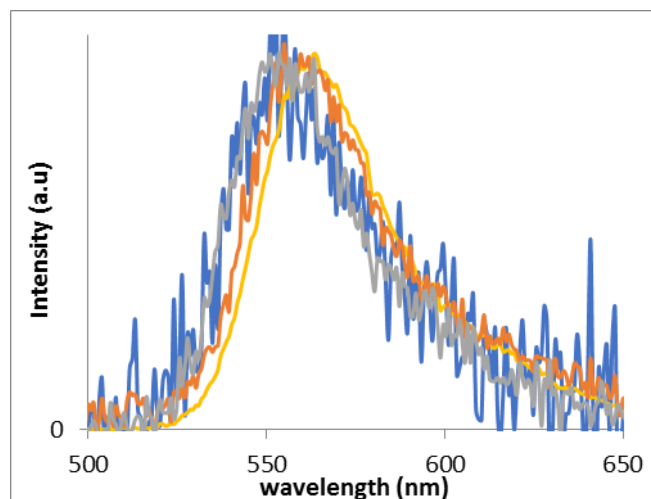
Figure 34. Fluorescence emission spectra of free R6G in aqueous solution, with PSS and both PE, PSS and PAH. Blue: R6G/DW; yellow: R6G/PSS/PAH 1:5:0,5; grey: R6G/PSS/PAH 1:5:5 and orange: R6G/PSS 1:5.

Although revealing to be very similar, the emission spectra showed a red-shift deviation in the systems with PSS, relatively to it's the systems where PSS was absent (figure 34). As the fluorescence assays performed before in the cuvette.

Resorting to FLIM, the TSPP-R6G was also studied. The temporal variation of the emission spectra seems to show the photodegradation of the acceptor molecule, the porphyrin (TSPP), whereby there will be less molecules extinguishing the donor molecules, rhodamine (R6G). This will cause the increasing of the R6G fluorescence signal. This process is mediated by the polyelectrolytes present in the solution, which have an essential role turning the distance between porphyrin and rhodamine molecules, as well as their dipoles orientation suitable for the Förster resonance energy transfer (figure 35).
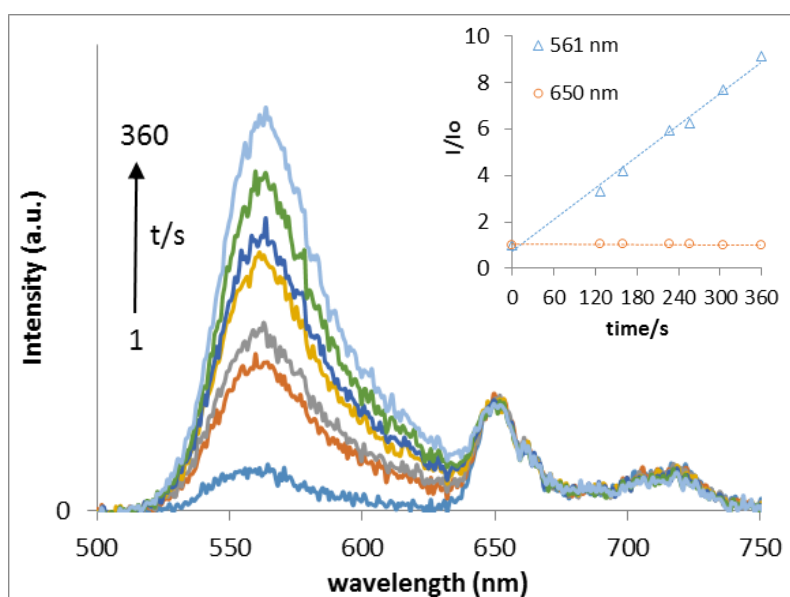


Figure 35. Fluorescence emission spectra of R6G/TSPP/PAH/PSS (1:1:2:2), obtained with $\lambda_{exc}$=483 nm at different excitation times (from 0s to 6 min). Inset shows the intensity variation with time for the $\lambda_{em}$=650 nm and $\lambda_{em}$=561 nm.
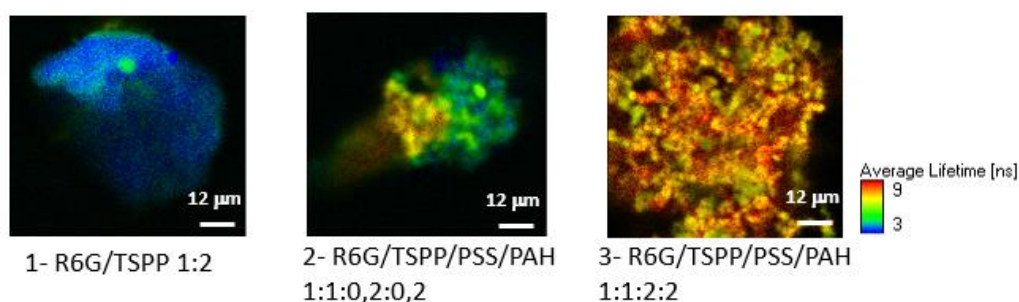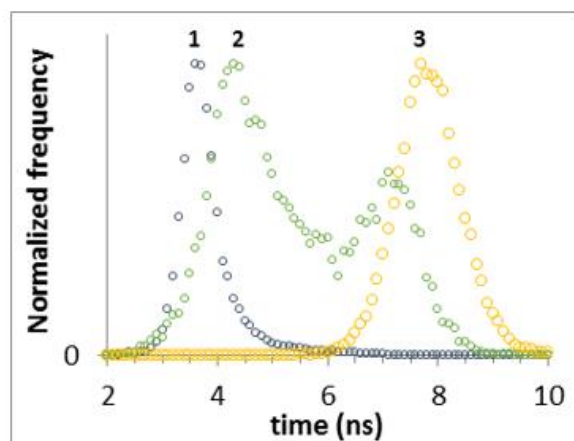
Figure 36. Fluorescence lifetime histogram of the systems 1- R6G/TSPP 1:1 in water; 2-R6G/TSPP/PSS/PAH 1:1:0,2:0,2 and 3- R6G/TSPP/PSS/PAH 1:1:2:2 and corresponding FLIM images.

The FLIM images, figure 36, show heterogeneity for the R6G/TSPP system, since there's occurrence of blue pixels associated with average lifetimes of about 3 ns and green pixels associated with average lifetimes of about 4 ns, which might be assigned to R6G molecules aggregated, probing hydrophobic surrounding and both monomeric rhodamine, respectively. The quantum yield of porphyrin was obtained through a relative determination method explained in the experimental methods section. As can be seen for the R6G/TSPP system in solution, there is no FRET process occurring: the rhodamine signal appears with a quantum fluorescence yield $\phi_{st} = 0.95$, higher than for TSPP, $\phi_x = 0.1$ .When polyelectrolytes are present in the solution, in higher concentrations (figure 36, 3), the distance between dipoles is the ideal for the efficiency of the FRET process, therefore only the acceptant molecule, TSPP, is detected (although preferably performing the excitation of the donor molecule, R6G). When polyelectrolytes are present in solution, but at low concentrations (figure 36, 2), there's lower efficiency of the FRET process, and some donor is still detected. The fluorescence lifetimes obtained by FLIM corroborate this, from table 5 it is shown that the prevalent population (36%) has a discrete lifetime of 10.3ns, which is the approximately the average lifetime of TSPP in its monomeric form at pH 7 in water.

Table 5. Fluorescence lifetimes of R6G and TSPP in aqueous solution with polyelectrolytes obtained by FLIM, λexc=483 nm; λem all range of λ above 510 nm.

| | $\tau_1$ | $A_1(\%)$ | $\tau_2$ | $A_2(\%)$ | $\tau_3$ | $A_3(\%)$ | $\chi^2$ |
|---|---|---|---|---|---|---|---|
| PSS/PAH | 4.9 | 33 | 10.3 | 36 | 1.26 | 32 | 1.256 |

Therefore, these are promising results for the next step of coating these dyes in MCs.

### 3.4. Preparation of Polyelectrolyte Microcapsules

To overcome the hydrophobic character and easy aggregation of porphyrins under physiological conditions, aiming the target accumulation selectivity for diseased tissues, colloidal carriers such as $CaCO_3$ particles were studied and functionalized in three different designs. Different species can be incorporated into the shell structure giving them unique tailored properties. Seeking the attainment of carriers with the possibility of being detected by imaging techniques, and therefore to allow knowing their localization as well as their accumulation in the organism, the MCs adsorbed the R6G dye, which displays a quantum fluorescence yield of about ~95% [52].This dye can be used as donor upon light absorption for excitation energy transfer mechanisms, like FRET. Besides the donor, an acceptor like TSPP, which can be excited by the excitation energy of R6G is needed for this process. The excited acceptor is the photosensitiser of PDT and undergoes intersystem crossing to the triplet state from where it can transfer its energy to molecular oxygen, ultimately producing reactive oxygen species that can then destroy tumor tissues. The orientation of the dipoles of both R6G and TSPP is controlled by the addition of polyelectrolytes PSS and PAH. All assembled systems consist in the $CaCO_3$ core colloidal template and polyelectrolyte matrix shell prepared with LbL technique, based on the electrostatic interaction. The layer number, sequence and type of PE is the same for each studied system until the last PSS layer, from which the systems differ. The systems (figure 37) entail negative template-(positive PE/negative PE)$_n$-(other molecules), where n designates the number of positive/negative PE adsorption cycles, rhodamine 6G and TSPP.
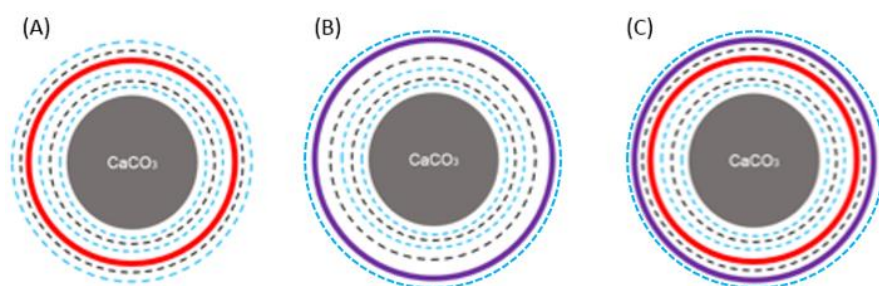


Figure 37. The structure of the three systems studied:
(A)CaCO₃(PSS)(PAH)(PSS)(R6G)(PAH)(PSS);
(B)CaCO₃(PSS)(PAH)(PSS)(PAH)(TSPP)(PSS);
(C)CaCO₃(PSS)(PAH)(PSS)(R6G)(PAH)(TSPP)(PSS).

Fabrication of homogenous CaCO3 particles is a significant step in assembling polyelectrolyte capsules. It is crucial to control the dimensions, the shape and the charge of the particles in order to have homogenously separated and charged templates as final result.

$CaCO_3$ colloidal particles are considered easily synthesisable, low cost of processing, and highly porous which leads to an increased loading capacity. However, their relatively big variation in size (polydispersity) and strong tendency to aggregate are some of the disadvantages of this kind of

templates. Biocompatibility tests for the $CaCO_3$ crystal structure vaterite particles indicated no cytotoxicity and no influence on viability or metabolic activity [53]. Synthesis of calcium carbonate templates is based on crystal growth of polycrystalline spherical vaterite particles precipitated by mixing of $CaCl_2$ (ion $Ca^{+2}$) and $Na_2CO_3$ (ion $CO_3^{-2}$) solutions. The final size of vaterite particles depends strongly on factors such as the concentration of both ions $Ca^{+2}$ and $CO_3^{-2}$, the reaction time, and the rotation speed during mixing.

Although vastly described in literature, the synthesis of CaCO3 particles with a narrow size distribution and with uniform shape is a sensitive process. (Sabri et al., 2015). There are two important steps in the preparation of $CaCO_3$ particles with such characteristics. 1) Rapid mixing of the two salt solutions of $CaCl_2$ and $Na_2CO_3$ that form clusters (reactive precipitation) and then left undisturbed for ten minutes, to obtain relatively similar size between particles. 2) Higher stirring speeds influence the uniformity and shape of the particles, to achieve a spherical shape and the 1.5µm-2µm size, a stirring speed of 1500 rpm had to be used. Others have claimed that decreasing the size of the particles to less than 4 µm, turns the average value of the pore size to 30–35 nm. [53][54].

After testing CaCO3 microparticle production within different stirring magnets in different diameter cylindrical flasks it was found that these parameters also influence the shape of the particles obtained. The size of the magnet which covers the total bottom area of the flat flask is the most suitable to maintain constant and uniform stirring, resulting in uniform size and shape of the microparticles.

In order to promote the stability of vaterite in relation to the other crystalline forms of CaCO3, the crystallization of CaCO3 was done in the presence of the negatively charged polyelectrolyte PSS. There is a very strong charge-controlled permeation for capsules templated on CaCO3 microparticles, which are prepared in the presence of PSS. These polyelectrolyte molecules are initially incorporated during fabrication of the CaCO3 crystal matrix and then are entrapped inside the microcapsules after core removal. Homogeneity of both the particle size and the surface morphology turns these particles suitable for being used as templates for multilayer deposition.[55]

Although possessing a negatively charged surface, due to their prior crystallization with PSS, the CaCO3 templates shown destabilized when the first added layer was the positive charged electrolyte PAH. [56] This might be explained by the strong interaction between the appositively charged polyelectrolytes. The first added layer was always the negatively charged PE, PSS. The LbL adsorption process for the PE shell formation is governed mostly by electrostatic interactions between PSS, as a strong polyanion, and PAH as a relatively weak polycation, this PE couple is sensitive to pH changes, which influence the inter-polyelectrolyte interactions. Both PE solutions were prepared at pH=6.4 with NaCl 0.5 M, [PAH]= 13 mg/mL [PSS]=3 mg/mL.

Another crucial parameter for a successful construction of PE uCaps by LbL technique is ionic strength. The increase of NaCl concentration on the PE solutions during LbL deposition results in

the thickening of the capsule shell. When salt concentrations are too high, it can shield interparticle electrostatic repulsions, which are needed to prevent aggregation. It has also been proposed that concentrations that are too low can lead to inflexibility of the PE chains, which wrap around the microparticle resulting in an inadequate or incomplete coating.[6]

On the other hand, the increase of the time of polymer deposition allows PE molecules to better fill in the internal pores of CaCO3 core and to form more polymer matrix in the capsule after the core removal. This is not accompanied by any changes in the thickness of the capsule wall. PE concentrations which are too low can lead to incomplete particle coverage and subsequent aggregation. Concentrations that are too high will lead to particle aggregation, especially when higher molecular weight PE are used (this occurs when the PE adsorbs on more than one particle, grouping the particles together). Since the molecular weight of the polyelectrolyte PAH (MW~17500) is considerably lower comparing to the PSS molecular weight (MW~75000), the PAH adsorption solution is more concentrated than the PSS solution for the adsorption of the negative polyelectrolyte layer.

The zeta potential indicates the potential stability of the system. If all the particles in suspension have a large negative or positive zeta potential then they will tend to repel each other, avoiding aggregation. However, if the particles have low zeta potential values there will be no force to prevent the particles coming together, creating aggregates. The general values between stable and unstable suspensions is generally taken at +30 or -30 mV. Particles with zeta potentials more positive than +30 mV or more negative than -30 mV are normally considered stable. However, if the particles have a density greater than the dispersant, even though they are dispersed, they will eventually sediment forming a pellet. [56][57]

Zeta potential was measured after the addition of each polyelectrolyte layer to assure the satisfactory inversion of the overall charge, upon the first layer of PSS the zeta potential obtained was $\zeta($ CaCO$_3$-PSS)=-18.1mV; after the addition of the positive charge PE, the value obtained was $\zeta($CaCO$_3$-PSS-PAH)=-11.5 mV. One addition of PAH was therefore inefficient to invert favourably the overall charge of the negative charged template. Two additions of PAH resulted in a $\zeta$ (CaCO$_3$-PSS-(PAH))=+8.3mV, still weakly positive for a stable colloidal system. Finally, after three additions of PAH the overall surface charge of the particle inverted, and its zeta potential was acceptable for the suspension to be stable, $\zeta($ CaCO$_3$-PSS-(PAH)) =+34.8mV, figure 38. The fourth addition of PAH proved not to be necessary for the little improvement of the positive charge $\zeta($CaCO$_3$-PSS-(PAH)) =+36.6 mV. The addition of PSS after three additions of PAH resulted in a zeta potential value of $\zeta($CaCO$_3$-PSS-(PAH)-PSS)=-34.7mV.
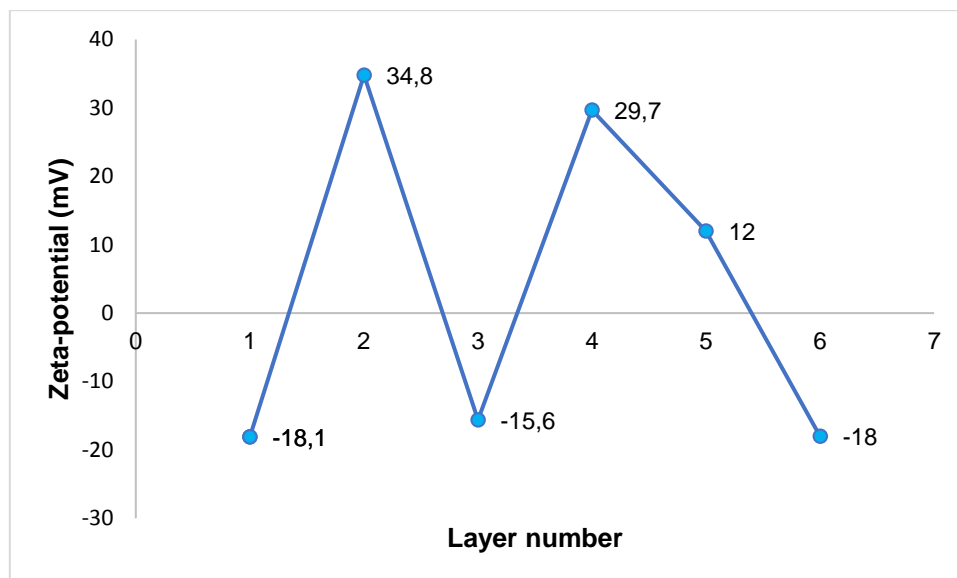
Figure 38. Zeta potential (ȝ) variation of the polyelectrolyte microcapsule, after the addition of each polyelectrolyte; PAH additions have a positive effect on the overall surface charge, and PSS additions have a negative effect on the overall surface charge. System $CaCO_3(PSS)(PAH)(PSS)(R6G)(PAH)(TSPP)(PSS)$.

The investigation of the stability of the crystals coated with different number of PSS/PAH layers revealed the optimal conditions for the formation of the microcapsules. It is known that storage of the vaterite crystals in water for long time (overnight or more) results in recrystallization of vaterite to more stable calcite polymorph. [58] Calcite crystals have typical cubic shape that allows to easy distinguish them from spherical vaterite crystals. The degree of recrystallization of vaterite crystals significantly drops down for three or more deposited polymer layers. This can be explained by stabilization of the crystals coated with the PE multilayers.

### 3.4.1. Systems Characterization

PE choice of layers determines the structure of the polymeric shell which is usually thick and appears as a polyelectrolyte network, compromising the system integrity. This matrix is used for the loading of molecules, here functionalized with R6G and porphyrin TSPP.

Although presenting a visual flattening, as seen in TEM images below (fig 39.), the capsules are usually not hollow inside but have a polymer complex in the internal lumen due to permeation of polymers through $CaCO_3$ crystal pores during the LbL coating procedure. An increase of the number of layers, leads to the strengthening of the capsule shell, this has been described as a factor that prevents capsule shrinkage during core dissolution with EDTA, which was not performed in this study. The shrinkage event takes place due to annealing the polymer structure into the formed capsules. This annealing is driven by closure of some voids between polymers, to create more ionic pairs in the polymer complex. The more layers deposited, the more pronounced is the shrinkage. The effect of the shrinkage can be completely eliminated for the capsules formed by more than five layers, however, in this case it has been reported that the dissolution of the core requires longer times. Altogether, this suggest that the optimal PSS/PAH capsules templated on the CaCO3 cores are assembled from four or five layers. Still, in the

experiments carried out and presented below, cores were not removed. The large thickness of the MCs with cores makes them appear very dark in TEM images, figure 39. Another side effect of absence of core removal is the increase of dispersed light by MCs suspensions. [59]
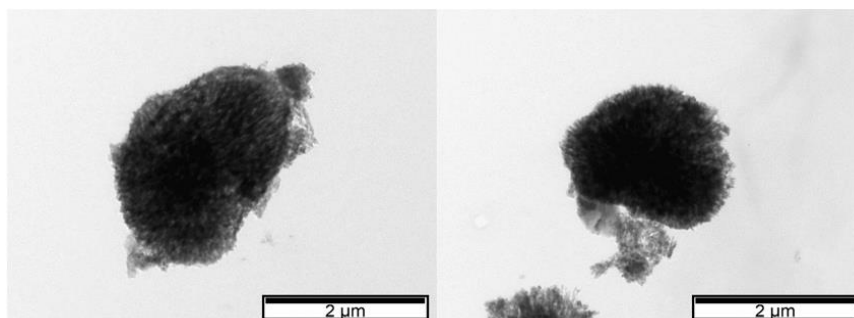


Figure 39. TEM images of CaCO₃(PSS)(PAH)(PSS)(PAH)(PSS).

### 3.4.1.1. System CaCO₃(PSS)(PAH)(PSS)(R6G)(PAH)(PSS)

The successful loading of R6G in the CaCO3(PSS)(PAH)$_3$ matrix was indicated both by ζ-potential ʒ( CaCO3-PSS-PAH-PSS-R6G)=-15,6 mV, absorbance spectra (figure 40) and FLIM fluorescence signal. Due to its cationic nature the rhodamine interacts with the anionic PE, but also since the last adsorbed layer on the colloidal template matrix was PAH, positive PE, there's a strong electrostatic attraction with PSS. One can assume that both R6G and PAH compete for binding to PSS, and therefore the loading of PSS/PAH multilayers with R6G may cause the weakening of interpolymer interaction and affect the structure of multilayer capsules. Meanwhile, the uncomplexed sulfonate groups of PSS also have the ability to load R6G molecules. Besides, the R6G molecule has a small size (MW 442) and a high diffusion coefficient of $D = 4.3 \times 10^{-10} m^2 s^{-1}$, that eliminates diffusional limitations and allows the post-loading of capsules with this dye. [6]
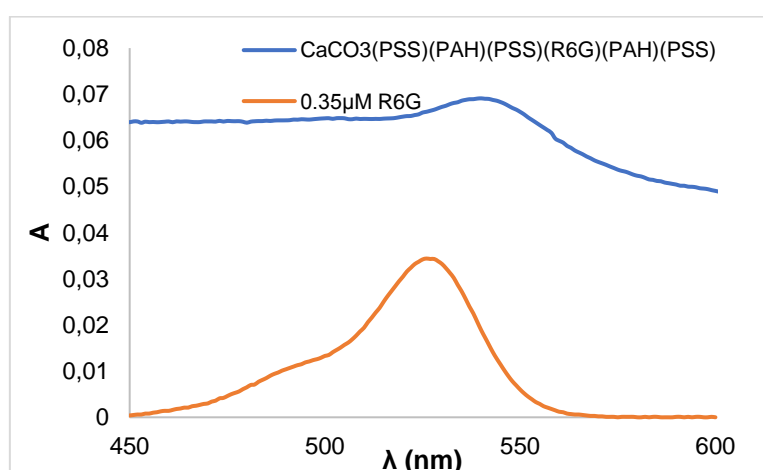


Figure 40. UV-Vis absorbance spectra of CaCO₃(PSS)(PAH)(PSS)(R6G)(PAH)(PSS) and 0.35 µM R6G in DW.

As seen in figure 40 there's a bathochromic shift of the maximum absorbance wavelength of R6G from ~526 nm to ~540 nm when adsorbed in the PE matrix, this is mainly due to the hydrophobicity change of the rhodamine, from the free aqueous solution to the MC polyelectrolyte matrix. This

effect have already been detected in the previous solution studies from which one could infer a strong hydrophobic interaction between PSS and R6G weakened the stacking interaction between bound dye cations. The relative small size of rhodamine chances the easy mobility in the PE matrix, towards the intrinsic layers of PSS, to prevent the contact with water molecules.

Table 6. Fluorescence lifetimes of R6G, TSPP and hybrid polyelectrolyte MCs obtained by $\lambda_{exc}$=483nm; $\lambda_{em}$ all range of $\lambda$ above 510 nm, $\lambda_{em}$=667-722 nm.

| Sample (exc=483nm; emi=510LP) | A1(%) | T1/ns | A2(%) | T2/ns | A3(%) | T3/ns | CHI |
|---|---|---|---|---|---|---|---|
| MCs R6G[*a] | 68 | 3.85 | --- | --- | 32 | 1.34 | 0.761 |
| MCs TSPP[*b] | --- | --- | 62 | 10.5 | 38 | 4.45 | 0.947 |
| MCs TSPP[*b] (exc=638nm; emi=667-722) | --- | --- | 63 | 10.2 | 37 | 3.65 | 1.046 |
| MCs Hyb[*c] | 36 | 3.35 | 18 | 10.9 | 46 | 1.33 | 1.006 |
| MCs Hyb[*c] (exc=638nm; emi=667-722) | 29 | 3.86 | 40 | 10.0 | 31 | 0.58 | 0.971 |

[*a] CaCO3(PSS)(PAH)(PSS)(R6G)(PAH)(PSS)

[*b] CaCO3(PSS)(PAH)(PSS)(PAH)(TSPP)(PSS)

[*c] CaCO3(PSS)(PAH)(PSS)(R6G)(PAH)(TSPP)(PSS)

The confocal microscopy images show round structures with an average diameter of ~2,5µm. From the FLIM images, c and d, it can be inferred that the rhodamine is homogeneously distributed in the MCs, green pixels (figure 41). The irregularity of shapes obtained is due to the template used, CaCO3.
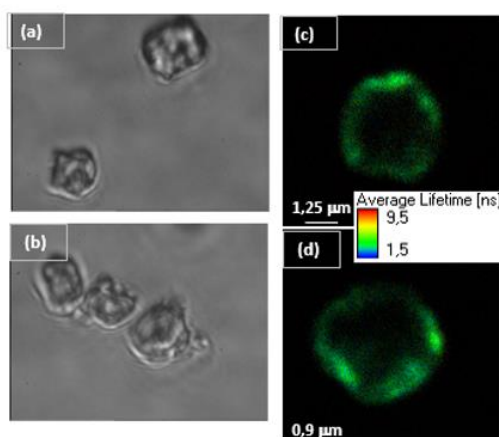


Figure 41. Confocal microscopy images (a, b) and FLIM images (c, d) of MCs with R6G (used ahead in releasing studies), obtained using laser excitation at $\lambda_{exc}$=483 nm.

### 3.4.1.2. System CaCO3(PSS)(PAH)(PSS)(PAH)(TSPP)(PSS)

The PE microcapsules were conveniently prepared with adsorption of TSPP. The UV-vis absorption, emission and FLIM results prove the efficient adsorption of the porphyrin onto PE matrix. Once again, the electrostatic force is responsible for the successful assembly of the system. TSPP exists as a tetranion at pH 8 and thereby can strongly bind with ammonium groups of the polyelectrolyte PAH. Incorporation of TPPS in the PE microcapsules led to a change in colour of the particles from white to faint red. In order to achieve a reversion of the zeta potential 1 mL of TSPP solution with 0,25mg/L was used, leading to a final value of -19.7 mV. Besides

decreasing further the zeta potential (-22.8 mV), the final addition of PSS also leads to changes in the preferential species of TSPP that is stabilized in the PE MCs, as it will be shown ahead. Figure 42 shows the porphyrin coated MCs, irregular round, with diameter of 2µM.
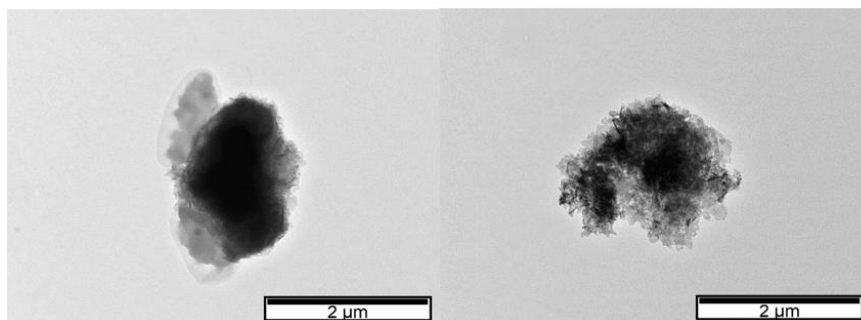


Figure 42. TEM images of CaCO$_3$(PSS)(PAH)(PSS)(PAH)(TSPP)(PSS) after release of the porphyrin, which will be studied in the next chapter of the discussion.
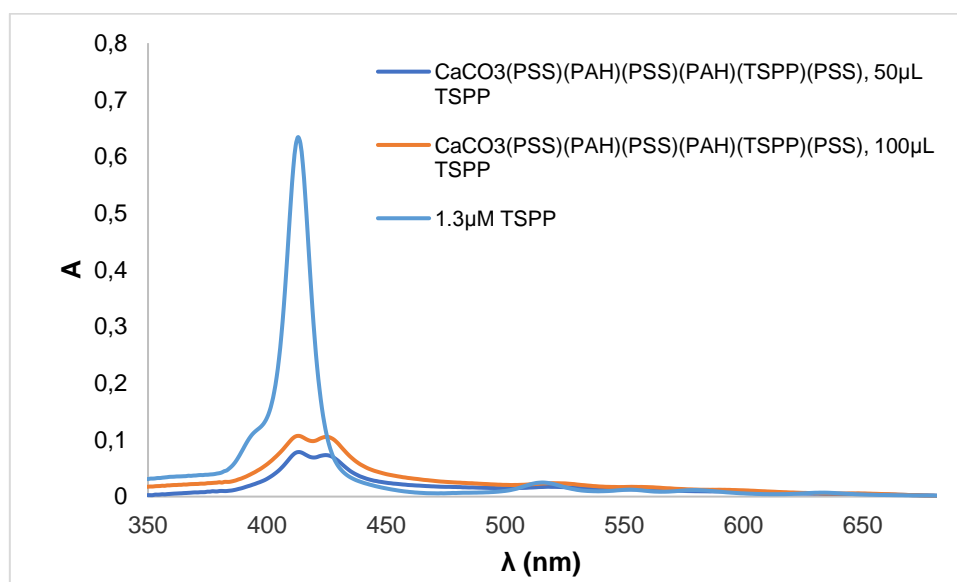


Figure 43. UV-Vis absorbance spectra of CaCO$_3$(PSS)(PAH)(PSS)(PAH)(TSPP)(PSS) at two different volumetric additions of porphyrin to the PE MCs: 50µL (dark blue) and 100µL (orange); 1.3µM TSPP aqueous solution absorbance signal at pH=7 (light blue).
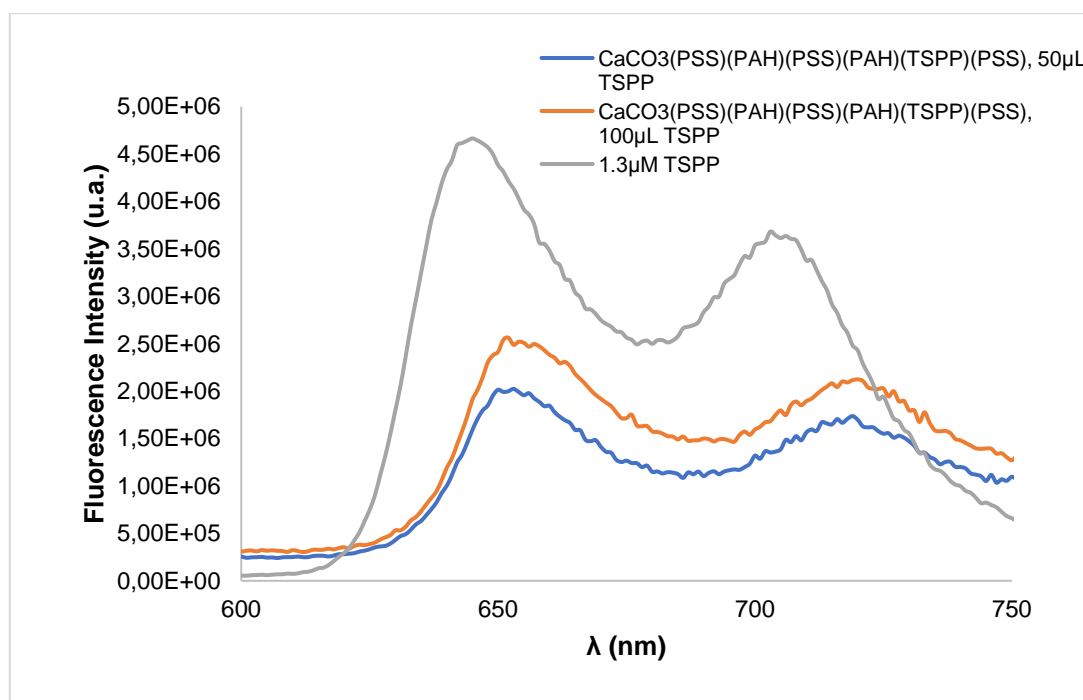
Figure 44. Emission spectra of CaCO$_3$(PSS)(PAH)(PSS)(PAH)(TSPP)(PSS), $\lambda_{exc}$=483 nm, pH=7.

The absorbance spectra of TSPP adsorbed to MC's PE matrix show that the duplication of the addition volume of porphyrin to the MCs does increase the absorbance signal proportionally, as well as for the emission signal. The behaviour of TSPP in PE MCs, is different from that observed in aqueous solution of polyelectrolytes. The adsorption of TSPP to the MCs in facilitated by the positive charges of PAH layer. Nonetheless, as observed in the absorption spectra in solution, H-aggregates are favoured. The addition of the final PSS layer, due to the important interaction of the two PE creates an environment in which H-aggregates are no longer stabilized. Under such conditions, TSPP absorption spectra depict 2 bands, one with maximum at 413 nm assignable to the monomer in an aqueous medium and another peak at ca. 426 nm. This previous results in aqueous solution shown that for the PAH-PSS 2µM (1:1) there's also a peak at 426 nm, which agree with the double shoulder peak shown above (figure 43 Therefore, PSS competition for PAH interactions changes the chain of the latter and displaces TSPP molecules. PAH chain becomes enlongated to allow connection through multi different binding sites, moving away and separating the TSPP molecules from each other. The emission spectra (figure 44) are in agreement with the changes reported in absorption, i.e., maxima at ca 556 and 718 nm similar to those obtained in the equimolar PAH-PSS mixture. In this instance, PSS effect is favourable to the MCs since disaggregates H-dimers of TSPP.

Fluorescence lifetimes of TSPP adsorbed to the assembled PE MCs (table 6) are in agreement with spectroscopic data. The best fitting to the decay was achieved with a 2-exponential model independently of the excitation laser used (483 or 638 nm). The long component, 10.2 ns, can be assigned to the monomer in an aqueous environment and it is the prevalent population in the system (63%). As for the short component, there is some variability in its value which can be understand by the heterogeneous and dynamic changes that are characteristic of the MCs.

Nonetheless, the lifetimes obtained are in the same order of those obtained for TSPP in presence of equimolar concentrations of PAH-PSS aqueous solutions (~4.8 ns, see table 2).
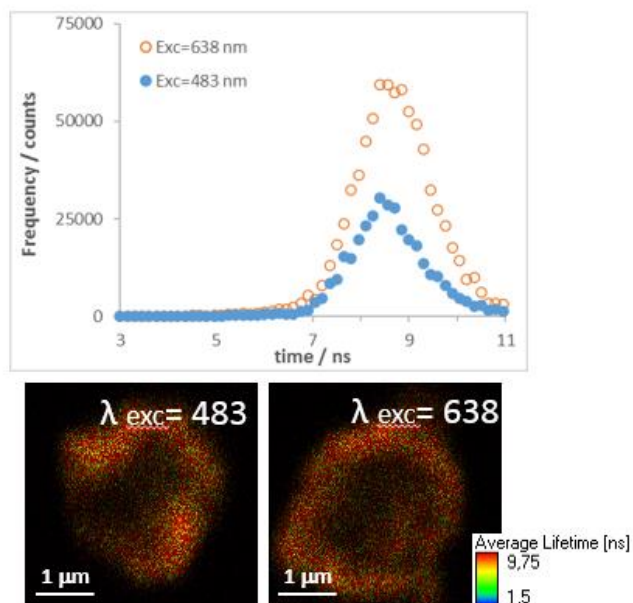


Figure 45. Fluorescence lifetime histograms obtained at $\lambda_{exc}$= 438 and $\lambda_{exc}$= 638 nm. FLIM images of polyelectrolyte microcapsules templated on CaCO3 microparticles, the microcapsules contain the following sequence of layers: CaCO3(PSS)(PAH)(PSS)(PAH)(TSPP). The hydrodynamic diameter is ~3.0 µm.

Both FLIM images, figure 45, show that TSPP is homogeneously distributed in the microcapsules, with average lifetime of 9.75ns agreeing well with the discussed before.

3.4.1.3. System CaCO3(PSS)(PAH)(PSS)(R6G)(PAH)(TSPP)(PSS)

In this section the hybrid system with both R6G and TSPP was studied. The PE microcapsules were conveniently prepared with adsorption of rhodamine/PSS aqueous solution, then PAH and then TSPP. The zeta potential measured on each addition and the emission results prove the efficient adsorption of both rhodamine and porphyrin onto PE matrix. Since the porphyrin will be released for treatment of diseased tissues, strategically the best design would be to adsorb this layer as a last step. The successful loading of R6G in the CaCO3(PSS)(PAH) matrix was indicated by ζ-potential, also, since the porphyrin will occupy the last adsorbed layer, to maintain the electrostatic cohesion a positive PE layer of PAH was adsorbed to the system, ʒ( CaCO3-PSS-PAH-PSS-R6G-PAH)=+29.7 mV. The zeta potential value measured for the hybrid system was ʒ(CaCO3-PSS-PAH-PSS-R6G-PAH-TSPP)=12 mV. As the decided order for the functionalization end up putting TSPP after R6G, aiming the easing of release of the porphyrin through media, it was decided to coat with a PSS layer at the end of the system to prevent aggregation of TSPP, ʒ(CaCO3-PSS-PAH-PSS-R6G-PAH-TSPP-PSS)=-18 mV. The TEM images for this system revealed microcapsules with approximately the same shape and size, figure 46.
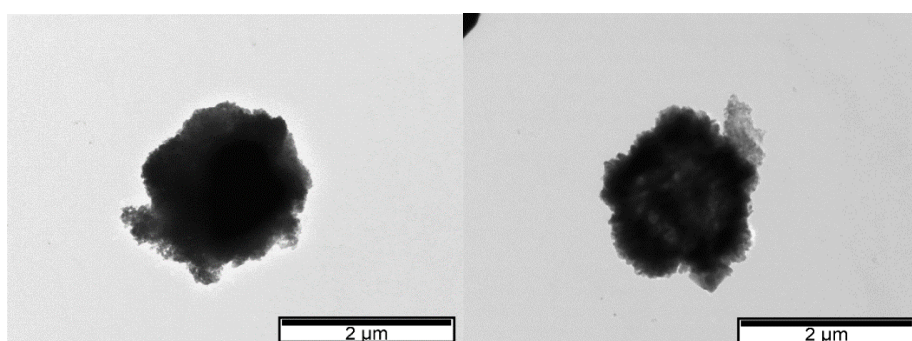


Figure 46. TEM images of CaCO3(PSS)(PAH)(PSS)(R6G)(PAH)(TSPP)(PSS).
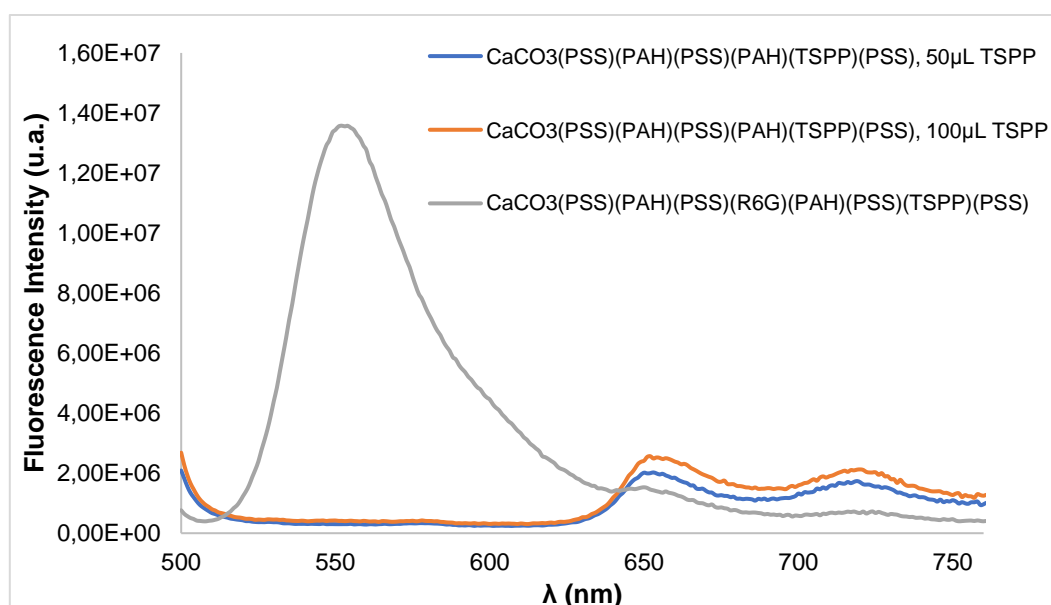
Figure 47. Emission spectra of CaCO3(PSS)(PAH)(PSS)(R6G)(PAH)(PSS)(TSPP), the hybrid system, and comparison with the porphyrin coated system λexc=483 nm, pH=7, slit 5/5 for the TSPP coated system (blue) and for hybrid system (orange).

The UV-Vis absorption spectra shown considerable light dispersion, and the impossibility to infer about absorption data. Since there's no abs data the ratio of fluorescence intensity and maximum OD, wasn't obtained. The emission spectra (figure 47) above show evidence that rhodamine was adsorbed to the capsule since its emission peak appears at ~556 nm. This value is in good agreement with that obtained for R6G in an aqueous solution of equimolar concentration of PAH-PSS (see figure, chap. 1). Two other quenched bands can be observed at ~650nm and ~720nm which correspond to the porphyrin emission bands in the CaCO3(PSS)(PAH)(PSS)(TSPP) system studied before, corroborating the porphyrin adsorption onto the MCs.

Fluorescence decays of the MCs containing the hybrid rhodamine – porphyrin molecules were obtained at two distinct excitation wavelengths, 483nm exciting preferentially R6G and 638 nm suitable for preferential excitation of TSPP (table 6). In both cases, a tri-exponential fitting was the one best describing the data. A long component around 10 ns can easily be assigned to the porphyrin in an aqueous environment. This component is the one prevailing at 638nm, as expected. The intermediate component can be assigned to R6G, the value of 3.86 is analogous to that of the dye alone in MCs, however, this component appears quenched in the hybrid upon excitation at 483 nm. This quenching can tentatively be assigned to a process of dynamic quenching taking place through energy transfer profiting from a suitable distance between the two probes provided by the assembly of the PE MCs. Under these conditions, the orientation of the donor emission dipole (R6G) and that of the acceptor absorption dipole (TSPP) is such that the energy transfer process is more efficient than the R6G radiative emission, leading to a quenching in R6G fluorescence emission. Another important characteristic of this system that further contributes to the prevalence of the resonance energy transfer is the important overlapping of the emission spectrum of the rhodamine and the absorption spectrum of TSPP [32]. The Förster critical radius, $R_0$, corresponds to the distance at which the rate constants $K_D$ and $k_{ET}$ are equal, such that energy transfer and spontaneous decay of the excited rhodamine are equally probable, also known as the distance at which the efficiency of energy transfer is 50%. The magnitude of Förster critical radius depends on the spectral properties of both R6G and acceptor molecules, TSPP. The expression of $R_0$, in angstroms (Å), is given by

$$R_0 = 0.2108[\kappa^2 \phi_D n^{-4} J(\lambda)]^{1/6} \quad (28)$$

Where $J(\lambda)$ is given in units of M-1cm-1nm4 if the wavelength $\lambda$ is expressed in nanometers, and represents the overlap integral of fluorescence emission spectrum of donor and absorption spectrum of acceptor, $\kappa^{-2}$ is the orientation factor for the emission and absorption dipoles and its value depends on their relative orientation, considering it random orientation it adopts the value of 2/3, $n$ the refractive index of the medium and $\phi_D$ the quantum yield of the donor (as introduced in section 2.1.5).

$$J(\lambda) = \int_0^\infty F_D(\lambda)\varepsilon_A(\lambda)\lambda^4 d\lambda \qquad (29)$$

$F_D(\lambda)$ is the fluorescence intensity of the donor in the absence of acceptor normalized so that $F_D(\lambda)d\lambda$ is 1, and $\varepsilon_A(\lambda)$ the molar extinction coefficient of the acceptor. The calculated $J(\lambda)$ is The quantum yield of the R6G molecule is 0.95 [51], $\kappa^2$ might be considered to be 2/3, n=1.5(PAH/PSS multilayers). With this, we can find the $R_0$, and then energy transfer rate constant $k_{ET}$ and efficiency of energy transfer $E$, by the equations 26 and 27 (see subsection 2.1.5).
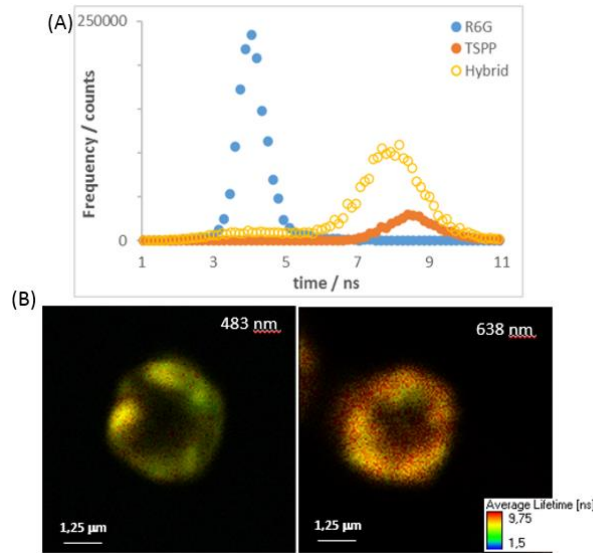


Figure 48. (A) Fluorescence lifetime histograms obtained at λexc= 438 for the hybrid MC samples, MCs functionalized with TSPP or with R6G (drop) were obtained in the same excitation conditions λexc=483 nm; (B) FLIM images of the hybrid MC sample (drop) obtained at two different excitation wavelengths, λexc=483 nm (left) and λexc=638 nm (right). The hydrodynamic diameter is ~3.5 µm.

Further evidence can be obtained from FLIM data, figure 48. Upon excitation at 483 nm, the donor molecules (R6G) are excited preferably, and the effect fluorescence quenching can be addressed between R6G and the acceptant molecules of the porphyrin TSPP, composing the FRET process. Comparing with the solution system studied in the first chapter, evaluating the energy transfer process within R6G and TSPP in the polyelectrolytes aqueous solution, the FRET process show signs of higher efficiency when occurring in the adsorbed layers of the MCs. This might be linked to the shortening distances between TSPP and R6G molecules in the PE matrix adsorbed to the CaCO3 templates.

### 3.5. Release of TSPP

The local concentration of TSPP is an important parameter to ensure the success of the efficiency of MCs as drug delivery systems. After discussing the adsorption of PE, rhodamine and porphyrin layers onto de MCs, it is also of importance to understand the assembled system behaviour in controlled surroundings which mimic the physiological environment. The hybrid CaCO3(PSS)(PAH)(PSS)(R6G)(PAH)(TSPP)(PSS) system, and CaCO3(PSS)(PAH)(PSS)(PAH)(TSPP) porphyrin system were studied.

For the release performed at physiological pH=7.2, the MCs were suspended in a salt release solution NaH2PO4.H2O 0,68% (w/v), under stirring with media renovation after each cycle of centrifugation and supernatant collection; mimicking intestinal environments. [60]

The mass of porphyrin released at a given time, $t$, is given by

$$Mass\ of\ porphyrin\ released = \sum Concentration(t) * V \quad (32)$$

Where $V$ is the collected volume of supernatant ~1mL, and the concentration (t) is given by

$$Concentration\ (t) = \frac{Abs\ (\lambda_{max})t}{\varepsilon b} \quad (33)$$

The %release is given by

$$\%release = \frac{Mass\ of\ porphyrin\ released}{Mass\ of\ porphyrin\ adsorbed} \times 100 \quad (34)$$

Where the mass of porphyrin adsorbed for each system was calculated before through the sum of lost TSPP during the washing steps of the MCs.

Table 7. Total amount of porphyrin released and %release observed for PE MCs in pH=7.2.

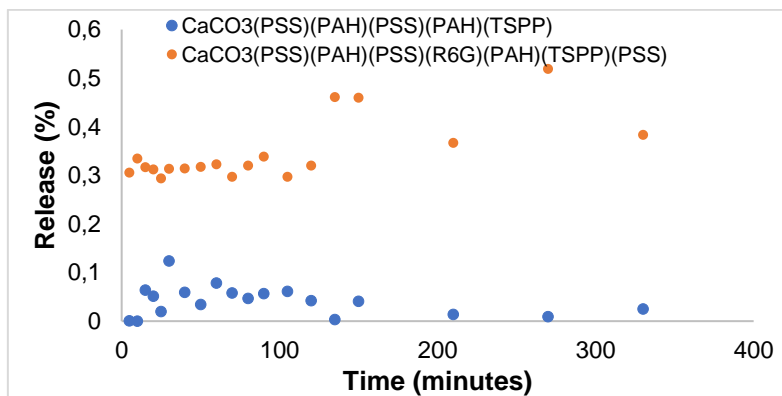| System | TSPP$_{release}$ (nmol) | % Release | $S = \sqrt{\sigma^2}$ |
|---|---|---|---|
| CaCO3(PSS)(PAH)3(PSS)(PAH)(TSPP)(PSS) | 0.277 | 0.6 | 0,0302 |
| CaCO3(PSS)(PAH)$_3$(PSS)(R6G)(PAH)(TSPP)(PSS) | 3.2 | 6.6 | 0,0623 |



Figure 49. Porphyrin release from CaCO3(PSS)(PAH)$_3$(PSS)(R6G)(PAH)(TSPP)(PSS) system, and CaCO3(PSS)(PAH)(PSS)(PAH)(TSPP) ($\lambda_{exc}$=483, $\lambda_{em}$=650).

The system CaCO$_3$(PSS)(PAH)(PSS)(R6G)(PAH)(TSPP)(PSS) is the one with higher released percentage of porphyrin through media surroundings, this quantity is high comparing with the total amount of porphyrin adsorbed for each system (0.03521µmol for the porphyrin system CaCO$_3$(PSS)(PAH)(PSS)(PAH)(TSPP)(PSS), and 0.0484µmol for the hybrid system CaCO$_3$(PSS)(PAH)(PSS)(R6G)(PAH)(TSPP)(PSS)).

For the hybrid system the fluorescence intensity values of the supernatants were obtained with λ$_{exc}$=483 nm, and converted in absorbance from a linear regression of fluorescence intensity versus concentration of porphyrin, and afterwards, using the Lambert-Beer Law (equation 11) to know the correspondent absorbances, and therefore, knowing that $\varepsilon = 5.1 \times 10^5 M^{-1} cm^{-1}$, the corresponding concentrations.

The points which release was found to be 0% correspond to collections of supernatants with no or residual presence of TSPP. In fact, the last collections of supernatant within the study of the hybrid MCs release shown long agitation time resulted in higher release, table 8 and figure 49.

Table 8. Conditions for each supernatant collection used in the release study.

| Collections | Agitation time (min) | Centrifugation time (min) |
|---|---|---|
| 1-6 | 1 | 4 |
| 7-12 | 4 | 4 |
| 13-16 | 11 | 4 |
| 17-19 | 56 | 2 |

The release of TSPP in a neutral pH media is not an efficient one, as indicated by the values obtained and presented in table 8. The porphyrin of the hybrid system is coated between layers of different charged PE, PAH and PSS orderly. For the matrix of these capsules it might be steadier for the system the affinity of both opposite charged polyelectrolytes to come closer in the matrix and to release some porphyrin into the media. Nevertheless, this quantity is very low (~6.6%) comparing with the adsorbed mass of porphyrin. The standard deviation is calculated as the square root of variance, the data associated to the release of porphyrin from hybrid MCs is more dispersed than the single functionalized TSPP MCs. As might be seen in the figures 50, both confocal microscopy and FLIM images after release (b) and (d) display a disorganized/ruptured structure.
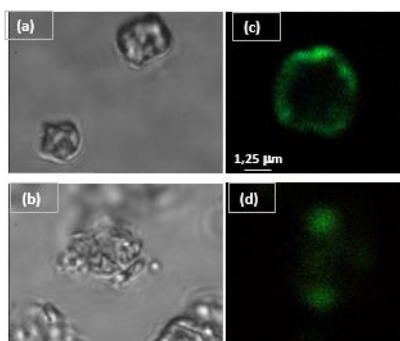


Figure 50. Confocal microscopy images (A and B) and FLIM images of hybrid MCs (C and D) obtained using laser excitation at λ$_{exc}$=483 nm.

4. General Conclusions and Future Remarks

The experimental work described in this Thesis is arranged in the temporal order of the sequential studies that have been done. The subjects range from the simple aqueous solution TSPP's and R6G's behaviour with polyelectrolytes, to layer-by-layer polyelectrolyte, rhodamine, and porphyrin colloidal coated templates of $CaCO_3$. Microcapsules' suspensions exhibit high degree of scattering, likely to introduce spectral artifacts, and their concentration reduction leads to undesirable reduction of the absorption signal, sometimes to undetectable levels. Nevertheless, the aqueous solutions of both porphyrin and rhodamine with polyelectrolytes may be taken as reference to study the interaction of these intervenient when assembled in the microcapsules. Yet, comparing emission intensities of identical sets of MCs seems reasonable. The issue here was the lack of a simple method to determine the concentration of MCs. $CaCO_3$ colloidal template revealed difficult to obtain regular sized spheres, related to its crystal structure. To attest the effective adsorption of each layer added to the MCs system and its stability, the zeta potential was measured after the addition of each polyelectrolyte and dye, to assure the satisfactory inversion of the overall charge. Three systems were designed, the porphyrin coated MCs, the rhodamine coated MCs and the hybrid, with both R6G and TSPP. For the use in PDT, the hybrid system maintain the monomer form of the porphyrin, adsorption onto the colloidal PSS and PAH matrix template prevented self-quenching, but the release of the porphyrin in neutral environments mimicking the intestinal region (followed at pH 7.2) shown high stability of the system with low release values. It is important to refer that other metabolic processes such as enzymatic activity, endocytosis or organism mechanical degrading mechanisms might as a hypothesis degrade the MCs, resulting in higher yielding release efficiencies when studying in vivo trials. The release of these MCs systems was not studied in acidic pHs, but some considerations can be done relying this future remark for the present experimental work. Low pH would eventually degrade de $CaCO_3$ core of the polyelectrolyte MCs, resulting in neutralization of the media pH and formation of $CO_2$, promoting the capsule collapse. The overall impact of this behaviour would be the promotion of the porphyrin release. In this Thesis, the $CaCO_3$ core wasn't destroyed by EDTA addition, the obtained TEM images shown large thickness of the MC's, and dark cores. This contributed for the light dispersion in MCs suspensions. The enhancement of the porphyrin's emission was observed. FLIM images revealed the existence of energy transference from the donor molecules of R6G entrapped in the PE matrix of the MCs and the acceptor molecules of TSPP, by FRET mechanism. Comparing with the same system in aqueous solution, in which there is no excitation energy transfer, the hybrid system pointed to the importance of the distance reduction between donor and acceptor molecules, and the strategic role of the polyelectrolyte matrix, orientating the transition dipole's of the rhodamine and the porphyrin in such a way that the FRET mechanism is efficient. When in vivo, the rhodamine, upon irradiation, would transfer its energy to the acceptor molecule of the porphyrin, which then follows a Type II photochemical process involving an energy transfer between excited triplet state of the PS and stable triplet oxygen, resulting in ROS that can evoke some cell death pathways. During the layer-by-layer assembly of the MCs, it was detected substantial loss of rhodamine in the washing steps, the electrostatic interaction with the PE matrix wasn't strong enough to prevent some detachment

of this small sized dye with high diffusion constant. In the future, the design of MCs with different templates, polyelectrolytes, as well as different dye/porphyrin couples might be interesting.

## 5. BIBLIOGRAPHY

[1] World Health Organization. (2018).Global cancer data. International. Agency for Research on. cancer, 13–15.

[2] Griffiths, J. I., Cohen, A. L., Jones, V., Salgia, R., Chang, J. T., & Bild, A. H. (2019). Opportunities for improving cancer treatment using systems biology. *Current opinion in systems biology*, *17*, 41–50.

[3] Tsolekile, N., Nelana, S., & Oluwafemi, O. S. (2019). Porphyrin as Diagnostic and Therapeutic Agent. *Molecules (Basel, Switzerland)*, *24*(14), 2669.

[4] del Mercato, L. L., Ferraro, M. M., Baldassarre, F., Mancarella, S., Greco, V., Rinaldi, R., & Leporatti, S. (2014). Biological applications of LbL multilayer capsules: from drug delivery to sensing. *Advances in colloid and interface science*, *207*, 139–154.

[5] Parakhonskiy, B. V., Yashchenok, A. M., Konrad, M., & Skirtach, A. G. (2014). Colloidal micro- and nano-particles as templates for polyelectrolyte multilayer capsules. *Advances in colloid and interface science*, *207*, 253–264.

[6] Jeannot, L., Bell, M., Ashwell, R., Volodkin, D., & Vikulina, A. S. (2018). Internal Structure of Matrix-Type Multilayer Capsules Templated on Porous Vaterite $CaCO_3$ Crystals as Probed by Staining with a Fluorescence Dye. *Micromachines*, *9*(11), 547.

[7] Sukhorukov, G. B; Dähne, L.; Hartmann, J.; Donath, E.; Möhwald, H. Controlled precipitation of dyes into hollow polyelectrolyte capsules based on colloids and biocolloids Adv. Mater. 2000, 12, 112-115.

[8] Miksa, B. (2016). Fluorescent Dyes Used in Polymer Carriers as Imaging Agents in Anticancer Therapy. *Medicinal Chemistry, 6*, 611-639.

[9] Svenskaya, Y. I., Pavlov, A. M., Gorin, D. A., Gould, D. J., Parakhonskiy, B. V., Sukhorukov, B. V., (2016). Photodynamic therapy platform based on localized delivery of photosensitizer by vaterite submicron particles. Colloids and Surfaces B: Biointerfaces, 146, 171–179.

[10] Sharma, V., & Sundaramurthy, A. (2020). Multilayer capsules made of weak polyelectrolytes: a review on the preparation, functionalization and applications in drug delivery. Beilstein journal of nanotechnology, 11, 508–532. https://doi.org/10.3762/bjnano.11.41

[11] Gallardo-Villagrán, M., Leger, D. Y., Liagre, B., & Therrien, B. (2019). Photosensitizers Used in the Photodynamic Therapy of Rheumatoid Arthritis. International journal of molecular sciences, 20(13), 3339.

[12] Van Straten, D., Mashayekhi, V., Brujin, H. S., Oliveira, S., Robinson, D. J. (2017). Oncologic photodynamic therapy: Basic principles, current clinical status and future directions. Cancers, 9(2), 1–54.

[13] Pushpan, S. K., Venkatraman, S., Anand, V. G., Sankar, J., Parmeswaran, D., Ganesan, S., & Chandrashekar, T. K. (2002). Porphyrins in photodynamic therapy - a search for ideal photosensitizers. Current medicinal chemistry. Anti-cancer agents, 2(2), 187–207.

[14] Imran, M., Ramzan, M., Qureshi, A. K., Khan, M. A., & Tariq, M. (2018). Emerging Applications of Porphyrins and Metalloporphyrins in Biomedicine and Diagnostic Magnetic Resonance Imaging. Biosensors, 8(4), 95.

[15] Sibrian-Vazquez, M.; Jensen, T. J.; Vicente, M. G. H. Synthesis, characterization, and metabolic stability of porphyrin-peptide conjugates bearing bifunctional signaling sequences. J. Med. Chem. 2008, 51, 2915−2923.

[16] Agostinis, P., Berg, K., Cengel, K. A., Foster, T. H., Girotti, A. W., Gollnick, S. O., Hahn, S. M., Hamblin, M. R., Juzeniene, A., Kessel, D., Korbelik, M., Moan, J., Mroz, P., Nowis, D., Piette, J., Wilson, B. C., & Golab, J. (2011). Photodynamic therapy of cancer: an update. CA: a cancer journal for clinicians, 61(4), 250–281.

[17] Nowis, D., Makowski, M., Stokłosa, T., Legat, M., Issat, T., & Gołab, J. (2005). Direct tumor damage mechanisms of photodynamic therapy. Acta biochimica Polonica, 52(2), 339–352.

[18] Q. Z. Zhang, J. He, W. M. Yu, Y. C. Li, Z. H. Liu, B. N. Zhou, Y. M. Liu, RSC. Med. Chem. 2020, 1-11. A promising anticancer drug: a photosensitizer based on the porphyrin skeleton

[19] Hlapisi, N., Motaung, T. E., Linganiso, L. Z., Oluwafemi, O.S., Songca, S. P. (2019). Encapsulation of Gold Nanorods with Porphyrins for the Potential Treatment of Cancer and Bacterial Diseases: A Critical Review. Bioinorganic Chemistry and Applications, 2019.

[20] Zhang, J., Jiang, C., Figueiró Longo, J. P., Azevedo, R. B., Zhang, H., Muehlmann, L. A. (2018). An updated overview on the development of new photosensitizers for anticancer photodynamic therapy. Acta Pharmaceutica Sinica B, 8(2), 137–146.

[21] Ormond, A. B., Freeman, H. S. (2013). Dye sensitizers for photodynamic therapy. Materials, 6(3), 817–840.

[22] Huang, H., Song, W., Rieffel, J., & Lovell, J. F. (2015). Emerging applications of porphyrins in photomedicine. Frontiers in physics, 3, 23.

[23] Gottfried, J. M. (2015). Surface chemistry of porphyrins and phthalocyanines. Surface Science Reports, 70(3), 259–379.

[24] M. Uttamlal, A.S. Holmes-Smith, The excitation wavelength dependent fluorescence of porphyrins, Chem. Phys. Lett. 454 (2008) 223–228.

[25] Tomohiro Hashimoto, Yoong-Kee Choe, Haruyuki Nakano, and Kimihiko Hirao Theoretical Study of the Q and B Bands of Free-Base, Magnesium, and Zinc Porphyrins, and Their Derivatives The Journal of Physical Chemistry A 1999 103 (12), 1894-1904

[26] Hollingsworth, J. V., Richard, A. J., Vicente, M. G., & Russo, P. S. (2012). Characterization of the self-assembly of meso-tetra(4-sulfonatophenyl)porphyrin (H(2)TPPS(4-)) in aqueous solutions. Biomacromolecules, 13(1), 60–72.

[27] Serra, V. V., Neto, N. G. B., Andrade, S. M., Costa, S. M. B. (2017). Core-Assisted Formation of Porphyrin J-Aggregates in pH-Sensitive Polyelectrolyte Microcapsules Followed by Fluorescence Lifetime Imaging Microscopy. Langmuir, 33(31), 7680–7691.

[28] Moreno-Villoslada, I., Fuenzalida, J. P., Tripailaf, G., Araya-Hermosilla, R., Pizarro, G., Marambio, O. G., & Nishide, H. (2010). Comparative study of the self-aggregation of rhodamine 6G in the presence of poly(sodium 4-styrenesulfonate), poly(N-phenylmaleimide-co-acrylic acid), poly(styrene-alt-maleic acid), and poly(sodium acrylate). The journal of physical chemistry. B, 114(37), 11983–11992.

[29] Bhattarai, N., Chemotherapeutic Applications of Rhodamine Based NanoGUMBOS, 2018, *LSU Doctoral Dissertations*. 4499.

[30] Stephanos, J., Addison, A., Electronic Spectroscopy, Electrons, Atoms, and Molecules in Inorganic Chemistry, Academic Press, 2017, pp. 585-645

[31] Levitus, M. Handbook of Fluorescence Spectroscopy and Imaging. From Ensemble to Single Molecules. Edited by Markus Sauer, Johan Hofkens and Jörg Enderlein. Angew. Chem. Int. Ed. 2011, 50, 9017–9018.

[32] Valeur, B. (2001). Molecular Fluorescence: Principles and Applications. Wiley-VCH Verlag GmbH & Co. KGaA.

[33] Lakowicz, J. R. (2006). Principles of Fluorescence Spectroscopy. Springer, 3rd edition.

[34] Andrews, D. L.; Curutchet, C.; Scholes, G. D. Resonance Energy Transfer: Beyond the Limits. Laser Photon. Rev. 2011, 5, 114− 123.

[35] Kaszuba, M., Corbett, J., Watson, F. M. N., Jones, A. (2010). High-concentration zeta potential measurements using light-scattering techniques. Philosophical Trasactions of the Royal Society A: Mathematical, Physical and Engineering Sciences, vol. 368(1927), 4439–4451.

[36] Bhattacharjee, S. (2016). DLS and zeta potential - What they are and what they are not. Journal of Controlled Release, 235, 337–351.

[37] Trautmann, S., Buschmann, V., Orthaus, S., Koberling, F., Ortmann, U. Fluorescence Lifetime Imaging (FLIM) in Confocal Microscopy Applications: An Overview. PicoQuant GmbH, 1–14.

[38] Tang, C. Y., Yang, Z. (2017). Transmission Electron Microscopy (TEM). Membrane Characterization, 145-159.

[39] Flegler, S. L., Heckman, J. W., Klomparens, K. L. (1994). Scanning and transmission electron

microscopy: an introduction. Choice Reviews, 31(8), 31-4353.

[40] Serra, S., Inteligent polymeric microcapsules of nano hybrids of porphyrin-gold to apply on Photodynamic Therapy and Bioimaging, 2019, IST.

[41] N.C. Maiti, M. Ravikanth, S. Mazumdar, and N. Periasamy, Fluorescence dynamics of noncovalently linked porphyrin dimers and aggregates, J. Phys. Chem. 99 (1995) 17192- 17197.

[42] O. Ohno, Y. Kaizu, and H. Kobayashi, J-aggregate formation of a water-soluble porphyrin in acidic aqueous-media, J. Chem. Phys. 99 (1993) 4128-4139.

[43] D.L. Akins, H.-R. Zhu, and C. Guo, Absorption and Raman-scattering by aggregated mesotetrakis(p-sulfonatophenyl)porphine J. Phys. Chem. 98 (1994) 3612-3618.

[44] N.C. Maiti, S. Mazumdar, and N. Periasamy, J- and H-aggregates of porphyrin-surfactant complexes: time-resolved fluorescence and other spectroscopic studies, J. Phys. Chem. B, 102 (1998) 1528-1538.

[45] I.E. Borissevitch, T.T. Tominaga, H. Imasato, and M. Tabak, Fluorescence and optical absorption study of interaction of two water soluble porphyrins with bovine serum albumin. The role of albumin and porphyrin aggregation, J. Luminesc. 69 (1996) 65-76.

[46] Kozel, S.V., Skosyrskaya, E.K. & Beklemishev, M.K. Kinetic methods for determining water-soluble polymers. J Anal Chem 63, 693–699 (2008)

[47] Teixeira, R., Serra, V.V., Paulo, P., Andrade, S., & Costa, S. (2015). Encapsulation of photoactive porphyrinoids in polyelectrolyte hollow microcapsules viewed by fluorescence lifetime imaging microscopy (FLIM). *RSC Advances, 5*, 79050-79060.

[48] S.M. Andrade, R. Teixeira, Sílvia M.B. Costa, A.J.F.N. Sobral. Self-aggregation of free base porphyrins in aqueous solution and in DMPC vesicles. Biophysical Chemistry, Elsevier, 2008, 133 (1-3)

[49] F. L. Arbeloa, I. L. Gonzalez, P. R. Ojeda and I. L. Arbeloa, J. Chem. Soc., Faraday Trans. 2, 1982, 78, 989.

[50] S.M. Andrade and S.M.B. Costa, Spectroscopic studies of water-soluble porphyrins with protein encapsulated in bis(2-ethylhexyl)sulfosuccinate (AOT) reverse micelles: aggregation versus complexation, Chem. Eur. J., 12 (2006) 1046-1057.

[50] S. Terdale, A. Tantray, Spectroscopic study of the dimerization of rhodamine 6G in water and different organic solvents, J. Mol. Liq. 225 (2017) 662–671, https://doi. org/10.1016/j.molliq.2016.10.090

[51] Moreno-Villoslada, I.; Fuenzalida, J. P.; Tripailaf, G.; ArayaHermosilla, R.; Pizarro, G. D. C.; Marambio, O. G.; Nishide, H. Comparative Study of the Self-Aggregation of Rhodamine 6G in the Presence of Poly(Sodium 4-Styrenesulfonate), Poly(N - Phenylmaleimide- Co -Acrylic Acid),

Poly(Styrene- Alt -Maleic Acid), and Poly(Sodium Acrylate). J. Phys. Chem. B 2010, 114 (37), 11983–11992.

[51] R. F. Kubin and A. N. Fletcher, J. Lumin. 27, 455 (1982).

[52] Parakhonskiy, B., Svenskaya, Y. I., Yashchenok, A., Fattah, H., Inozemtseva, O., Tessarolo, F., Antolini, R., et al. (2014). Size controlled hydroxyapatite and calcium carbonate particles : synthesis and their application as templates for SERS platform. Colloinds and Surfaces, 118, 243–248.

[53] Wang, C., He, C., Tong, Z., Liu, X., Ren, B., Zeng, F. (2006). Combination of adsorption by porous CaCO3 microparticles and encapsulation by polyelectrolyte multilayer films for sustained drug delivery. International Journal of Pharmaceutics, 308(1–2), 160–167.

[54] Sabri, I. N., Alias, N., Ali, A. M., Mohammed, J. S. (2016). Characterization of CaCO3 microspheres fabricated using distilled water. The Malaysian Journal of Analytical Sciences, 20(2), 423–435.

[55] Maleki Dizaj, S., Barzegar-Jalali, M., Zarrintan, M. H., Adibkia, K., Lotfipour, F. (2015) Calcium carbonate nanoparticles as cancer drug delivery system. Expert Opinion Drug Delivery, 12(10), 75 1649–1660.

[56] Bhattacharjee, S. (2016). DLS and zeta potential - What they are and what they are not. Journal of Controlled Release, 235, 337–351.

[57] Fuller, M., Köper, I. (2018). Polyelectrolyte-coated gold nanoparticles: The effect of salt and polyelectrolyte concentration on colloidal stability. Polymers, 10(12).

[58] Bots, P.; Benning, L.G.; Rodriguez-Blanco, J.-D.; Roncal-Herrero, T.; Shaw, S. Mechanistic Insights into the Crystallization of Amorphous Calcium Carbonate (ACC). Cryst. Growth Des. 2012, 12, 3806–3814

[59] Teixeira, R., Optical Spectroscopy and Imaging of Porphyrins and Phthalocyanines: Self-Aggregation, Microencapsulation and Plasmon Enhanced Emission, 2012, IST.

[60] Neto, N., Construction of Polyelectrolyte Microcapsules envisaging potential Cancer Therapy, 2017, IST.